

# **A Nonresonant Technique to Estimate the Mechanical Material Properties of a Viscoelastic Cylinder**

**Andrew J. Hull**  
Submarine Sonar Department



**Naval Undersea Warfare Center Division  
Newport, Rhode Island**

## **PREFACE**

This report was prepared under Project No. 621Y250, "Hull Array Innovative Demonstration," principal investigator Pierre J. Corriveau (Code 213).

The technical reviewer for this report was David A. Hurdis (Code 2141).

The author wishes to thank Karen Holt (Code 543) for her help with the editing of the manuscript.

**Reviewed and Approved: 10 January 2001**



**Ronald J. Martin**  
**Head, Submarine Sonar Department**



# REPORT DOCUMENTATION PAGE

Form Approved  
OMB No. 0704-0188

Public reporting for this collection of information is estimated to average 1 hour per response, including the time for reviewing instructions, searching existing data sources, gathering and maintaining the data needed, and completing and reviewing the collection of information. Send comments regarding this burden estimate or any other aspect of this collection of information, including suggestions for reducing this burden, to Washington Headquarters Services, Directorate for Information Operations and Reports, 1215 Jefferson Davis Highway, Suite 1204, Arlington, VA 22202-4302, and to the Office of Management and Budget, Paperwork Reduction Project (0704-0188), Washington, DC 20503.

1. AGENCY USE ONLY (Leave blank)

2. REPORT DATE  
10 January 2001

3. REPORT TYPE AND DATES COVERED

4. TITLE AND SUBTITLE

A Nonresonant Technique to Estimate the Mechanical Material Properties of a Viscoelastic Cylinder

5. FUNDING NUMBERS

6. AUTHOR(S)

Andrew J. Hull

7. PERFORMING ORGANIZATION NAME(S) AND ADDRESS(ES)

Naval Undersea Warfare Center Division  
1176 Howell Street  
Newport, RI 02841-1708

8. PERFORMING ORGANIZATION  
REPORT NUMBER

TR 11,261

9. SPONSORING/MONITORING AGENCY NAME(S) AND ADDRESS(ES)

10. SPONSORING/MONITORING  
AGENCY REPORT NUMBER

11. SUPPLEMENTARY NOTES

12a. DISTRIBUTION/AVAILABILITY STATEMENT

Approved for public release; distribution is unlimited.

12b. DISTRIBUTION CODE

13. ABSTRACT (Maximum 200 words)

This report describes an innovative method for measuring the complex Young's modulus, complex shear modulus, and complex Poisson's ratio of a viscoelastic cylinder. The new nonresonant technique is based on measured transfer functions that are obtained by vibrating the cylinder linearly and rotationally with two different-size masses on its free end. Both masses have their own individual transfer functions, which can be measured and combined to yield the unknown Young's modulus and shear modulus values at every frequency where a measurement is made. Once these moduli are determined, Poisson's ratio can be calculated. The test method is subjected to Monte Carlo simulations to show that it is relatively unaffected by external noise in the data.

14. SUBJECT TERMS

Static/dynamic structural responses  
Material property estimates

Nonresonant measurement techniques  
Young's modulus

Shear modulus  
Poisson's ratio

15. NUMBER OF PAGES  
56

16. PRICE CODE

17. SECURITY CLASSIFICATION  
OF REPORT  
UNCLASSIFIED

18. SECURITY CLASSIFICATION  
OF THIS PAGE  
UNCLASSIFIED

19. SECURITY CLASSIFICATION  
OF ABSTRACT  
UNCLASSIFIED

20. LIMITATION OF ABSTRACT  
SAR

## TABLE OF CONTENTS

	Page
LIST OF TABLES .....	ii
1 INTRODUCTION.....	1
2 MEASUREMENT OF YOUNG'S MODULUS.....	3
3 NUMERICAL SIMULATION OF YOUNG'S MODULUS MEASUREMENT.....	9
4 MEASUREMENT OF SHEAR MODULUS .....	21
5 NUMERICAL SIMULATION OF SHEAR MODULUS MEASUREMENT.....	27
6 MEASUREMENT OF POISSON'S RATIO.....	39
7 CONCLUSIONS AND RECOMMENDATIONS.....	45
8 REFERENCES.....	47

## LIST OF ILLUSTRATIONS

Figure	Page
1 Laboratory Configuration for Measuring Young's Modulus .....	4
2 Magnitude and Phase Angle for Transfer Functions $T_1$ and $T_2$ Versus Frequency .....	10
3 Function $s$ Versus Frequency .....	11
4 Real and Imaginary Young's Modulus Values Versus Frequency .....	12
5 Magnitude and Phase Angle for Transfer Functions $T_1$ and $T_2$ With Noise Versus Frequency.....	15
6 Function $s$ With and Without Noise Versus Frequency .....	16
7 Real and Imaginary Young's Modulus Values Calculated With Noise Versus Frequency.....	17
8 Young's Modulus Estimation Error ( $\epsilon$ ) Versus Frequency.....	19
9 Laboratory Configuration for Measuring Shear Modulus.....	22

## LIST OF ILLUSTRATIONS (Cont'd)

Figure	Page
10 Magnitude and Phase Angle for Transfer Functions $S_1$ and $S_2$ Versus Frequency .....	28
11 Function $r$ Versus Frequency .....	29
12 Real and Imaginary Shear Modulus Values Versus Frequency .....	31
13 Magnitude and Phase Angle for Transfer Functions $S_1$ and $S_2$ With Noise Versus Frequency.....	33
14 Function $r$ With and Without Noise Versus Frequency.....	34
15 Real and Imaginary Shear Modulus Values Calculated With Noise Versus Frequency.....	35
16 Shear Modulus Estimation Error ( $\epsilon$ ) Versus Frequency .....	38
17 Real and Imaginary Poisson's Ratio Values Calculated Without Noise Versus Frequency .....	41
18 Real and Imaginary Poisson's Ratio Values Calculated With Noise Versus Frequency.....	42
19 Poisson's Ratio Estimation Error ( $\epsilon$ ) Versus Frequency.....	44

## LIST OF TABLES

Table	Page
1 Value of $n$ Versus Frequency .....	11
2 Transfer Function Error Versus Young's Modulus Estimation Error .....	18
3 Value of $m$ Versus Frequency .....	30
4 Transfer Function Error Versus Shear Modulus Estimation Error.....	37
5 Transfer Function Error Versus Poisson's Ratio Estimation Error .....	43

# **A NONRESONANT TECHNIQUE TO ESTIMATE THE MECHANICAL MATERIAL PROPERTIES OF A VISCOELASTIC CYLINDER**

## **1. INTRODUCTION**

Measuring the Young's modulus, shear modulus, and Poisson's ratio of materials is important because these parameters contribute significantly to the static and dynamic response of a structure.

Resonant techniques [1-7], which have been used to identify and measure moduli for many years, are based on comparing the measured eigenvalues of a structure to predicted eigenvalues from a model of the same structure. One limitation is that the model of the structure must have well-defined (typically closed-form) eigenvalues. A second concern is that resonant techniques allow measurements only at natural frequencies.

Comparison of analytical models to measured frequency response functions [8-12] is another approach for estimating the mechanical properties (stiffness and loss) of a structure. When the analytical model agrees with one or more frequency response functions, the parameters used to calculate the analytical model are considered accurate. However, if the analytical model is formulated with a numerical method, a comparison of the model to the data can be difficult due to the dispersion properties of the materials.

Other methods that measure Young's modulus require strain gauges [13-14] to be affixed to the cylindrical test specimen. However, the mounting of such gauges, which normally requires that the gauge be glued to the specimen, stiffens the material locally, causing an especially adverse impact on the estimate of stiffness and loss for soft viscoelastic materials.

Still another technique for measuring stiffness and loss is to deform the material and measure the resistance to the indentation [15]. The drawback here is that the specimen can be physically damaged if the deformation causes the sample to enter the plastic region of deformation.

This report describes the development of a nonresonant inverse method for measuring the complex Young's modulus and complex shear modulus of a cylindrical test specimen containing a mass on its end. The technique is best used when the end mass will change the dynamic response of the system, which typically occurs when an end accelerometer that measures response is attached to the test specimen. (It should be noted that the larger the mass, the more significant will be the response of the specimen.)

In the next sections, the linear and angular equations of motion for the test specimen with the mass are derived. The inverse method allows two sets of experimental measurements in the form of transfer functions to be recorded for both the linear and rotational configurations. These sets are combined to yield closed-form values of Young's modulus and shear modulus at each frequency for which a measurement is made. The calculation of Poisson's ratio, based on a material constitutive equation, can then be made from these previous measurements of moduli.

## 2. MEASUREMENT OF YOUNG'S MODULUS

Measuring the Young's modulus of the test specimen begins by mounting one end of the specimen to a mechanical shaker and attaching the other end to a mass. Next, one accelerometer is attached to the shaker head and a second is attached to the end-mounted mass, with the measurement axis of both accelerometers in the  $x$  direction. The laboratory configuration for this experiment is shown in figure 1. As can be seen from the figure, the shaker inputs energy into the test specimen in the form of a linear translation that initiates a compressional wave. The speed and loss of this wave is measured with the two accelerometers, and Young's modulus is then calculated from the result. This measurement (estimation) process is further described below.

The system model represents the test specimen (bar) attached to the mechanical shaker at  $x = 0$  and the mass at  $x = L$ , with the two attached accelerometers measuring the acceleration levels at each end of the bar. The linear, second-order wave equation modeling displacement in the bar is

$$\frac{\partial^2 u(x,t)}{\partial t^2} - \frac{E}{\rho} \frac{\partial^2 u(x,t)}{\partial x^2} = 0, \quad (1)$$

where  $u(x,t)$  is the axial particle displacement at location  $x$  (m) and time  $t$  (s),  $\rho$  is the density of the bar ( $\text{kg/m}^3$ ), and  $E$  is the unknown frequency-dependent, complex Young's modulus of elasticity ( $\text{N/m}^2$ ), which is yet to be determined. The boundary at  $x = 0$  is modeled as a fixed end with harmonic motion and is expressed as

$$u(0,t) = U_0 \exp(i\omega t), \quad (2)$$

where  $\omega$  is the frequency of excitation (rad/s),  $U_0$  is the amplitude (m), and  $i$  is the square root of -1. The boundary at  $x = L$  is formulated by matching the force at the end of the bar to the end mass multiplied by its linear acceleration and is expressed as

$$AE \frac{\partial u(L,t)}{\partial x} = -m \frac{\partial^2 u(L,t)}{\partial t^2}, \quad (3)$$



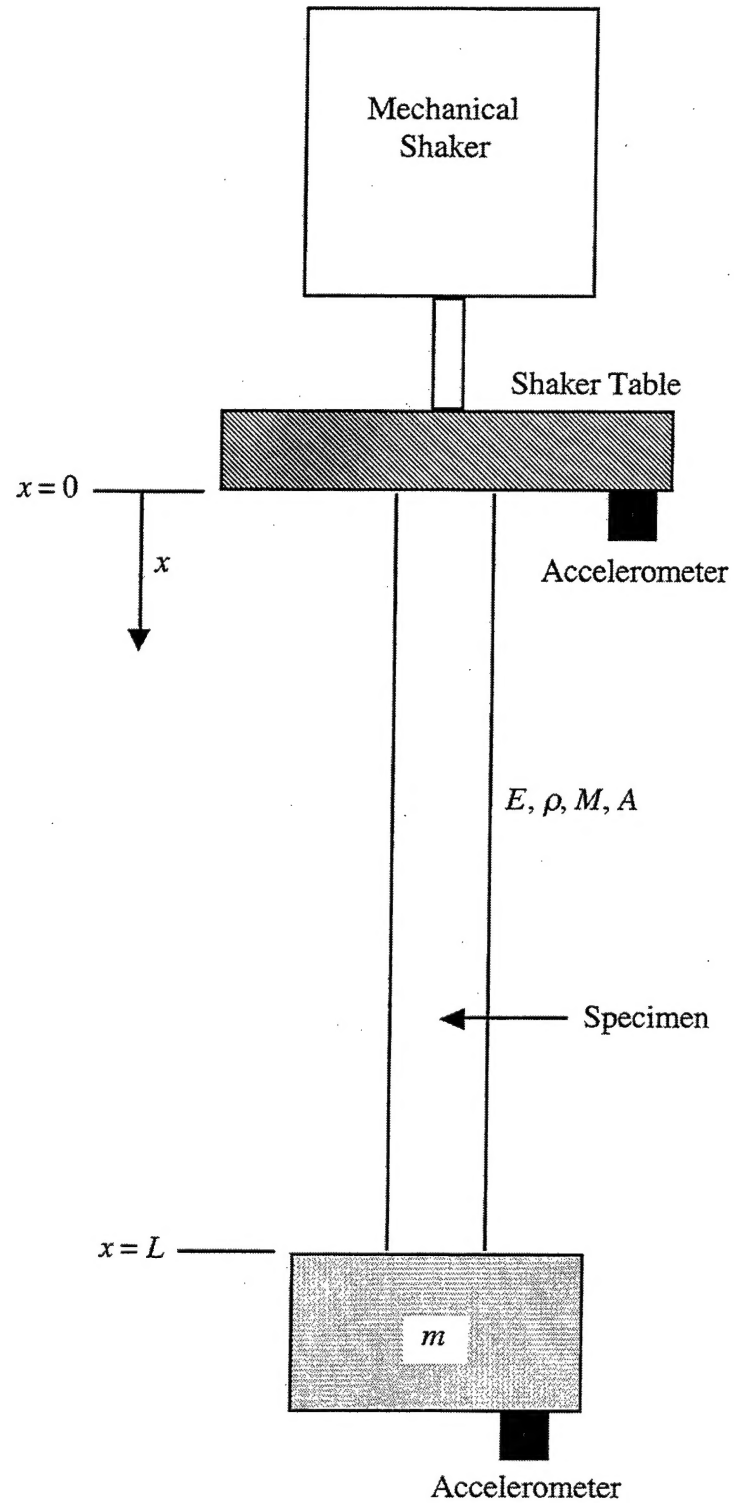


*Figure 1. Laboratory Configuration for Measuring Young's Modulus*

where  $A$  is the cross-sectional area of the bar ( $\text{m}^2$ ) and  $m$  is the mass at the end of the bar (kg).

Equation (1) can be rewritten in the spatial domain as

$$\frac{d^2 U(x, \omega)}{dx^2} + k_E^2 U(x, \omega) = 0 , \quad (4)$$

where  $U(x, \omega)$  is the temporal Fourier transform of the axial displacement and  $k_E$  is the complex compressional wavenumber (rad/m), which is equal to

$$k_E = \omega / \sqrt{E/\rho} . \quad (5)$$

Similarly, equation (2) becomes

$$U(0, \omega) = U_0 , \quad (6)$$

and equation (3) becomes

$$AE \frac{dU(L, \omega)}{dx} = m\omega^2 U(L, \omega) . \quad (7)$$

The solution to equation (4) is

$$U(x, \omega) = R(\omega) \cos(k_E x) + S(\omega) \sin(k_E x) , \quad (8)$$

where  $R$  and  $S$  are wave propagation constants. Applying boundary conditions (6) and (7) to equation (8) and then writing the solution as a transfer function in the form of a ratio between the displacement at both ends produces

$$\frac{U(L, \omega)}{U_0} = \left[ \frac{1}{\cos(k_E L) - \mu(k_E L) \sin(k_E L)} \right] , \quad (9)$$

where  $\mu$  is the ratio of the attached mass to the bar mass and is equal to

$$\mu = \frac{m}{M} , \quad (10)$$

where  $M$  is the mass of the bar (kg) expressed as

$$M = \rho AL . \quad (11)$$

The transfer function in equation (9) represents experimental data and is a function of unknown wavenumber  $k_E$ . The inversion of the two transfer functions obtained from the different attached masses will allow both sets of data to be combined, yielding a closed-form solution of  $k_E$  and then  $E$  as a function of  $\omega$ . The theoretical forms of these transfer functions are

$$\frac{U(L, \omega)}{U_0} = T_1(\omega) = \left[ \frac{1}{\cos(k_E L) - \mu_1(k_E L) \sin(k_E L)} \right] \quad (12)$$

and

$$\frac{U(L, \omega)}{U_0} = T_2(\omega) = \left[ \frac{1}{\cos(k_E L) - \mu_2(k_E L) \sin(k_E L)} \right] , \quad (13)$$

where the subscript 1 denotes the first attached mass and the subscript 2 denotes the second attached mass. Although the theoretical forms given in equations (12) and (13) are end displacement divided by input displacement, the transfer function created by end acceleration divided by input acceleration (obtained from the accelerometers) is identical in the frequency domain. Writing equations (12) and (13) as a function of  $(k_E L) \sin(k_E L)$  and then equating them yields

$$\cos(k_E L) = \frac{T_2 \mu_2 - T_1 \mu_1}{T_1 T_2 (\mu_2 - \mu_1)} = \phi , \quad (14)$$

where  $\phi$  is a complex quantity. The inversion of equation (14) allows the complex wavenumber to be solved as a function of  $\phi$ . The solution to the real part of  $k_E$  is

$$\text{Re}(k_E) = \begin{cases} \frac{1}{2L} \text{Arccos}(s) + \frac{n\pi}{2L} & n \text{ even} \\ \frac{1}{2L} \text{Arccos}(-s) + \frac{n\pi}{2L} & n \text{ odd} \end{cases}, \quad (15)$$

where

$$s = [\text{Re}(\phi)]^2 + [\text{Im}(\phi)]^2 - \sqrt{\{[\text{Re}(\phi)]^2 + [\text{Im}(\phi)]^2\}^2 - \{2[\text{Re}(\phi)]^2 - 2[\text{Im}(\phi)]^2 - 1\}}, \quad (16)$$

$n$  is a non-negative integer, and capital A denotes the principal value of the inverse cosine function. The value of  $n$  is determined from the function  $s$ , which is a cosine function with respect to frequency. At zero frequency,  $n$  is 0. Every time  $s$  cycles through  $\pi$  radians ( $180^\circ$ ),  $n$  is increased by 1. After the solution to the real part of  $k_E$  is found, the solution to its imaginary part is written as

$$\text{Im}(k_E) = \frac{1}{L} \log_e \left\{ \frac{\text{Re}(\phi)}{\cos[\text{Re}(k_E)L]} - \frac{\text{Im}(\phi)}{\sin[\text{Re}(k_E)L]} \right\}. \quad (17)$$

Once the real and imaginary parts of wavenumber  $k_E$  are known, the complex-valued modulus of elasticity can be determined at each frequency with

$$E(\omega) = \text{Re}[E(\omega)] + i \text{Im}[E(\omega)] = \frac{\rho \omega^2}{[\text{Re}(k_E) + i \text{Im}(k_E)]^2}. \quad (18)$$

Equations (12)-(18) produce an estimate of Young's modulus at every frequency for which a measurement is made.

### 3. NUMERICAL SIMULATION OF YOUNG'S MODULUS MEASUREMENT

Numerical simulations conducted to determine the effectiveness of this method use the following parameters to define a baseline problem:  $M = 4.0$  kg,  $m_1 = 0.4$  kg,  $m_2 = 1.2$  kg,  $L = 0.254$  m,  $\rho = 1200$  kg/m<sup>3</sup>,  $\text{Re}(E) = 10^8 + 10^5 f$  N/m<sup>2</sup>, and  $\text{Im}(E) = 10^7 + 10^4 f$  N/m<sup>2</sup>, where  $f$  is frequency in Hertz. From these values, the mass ratios  $\mu_1$  and  $\mu_2$  are computed to be 0.1 and 0.3, respectively.

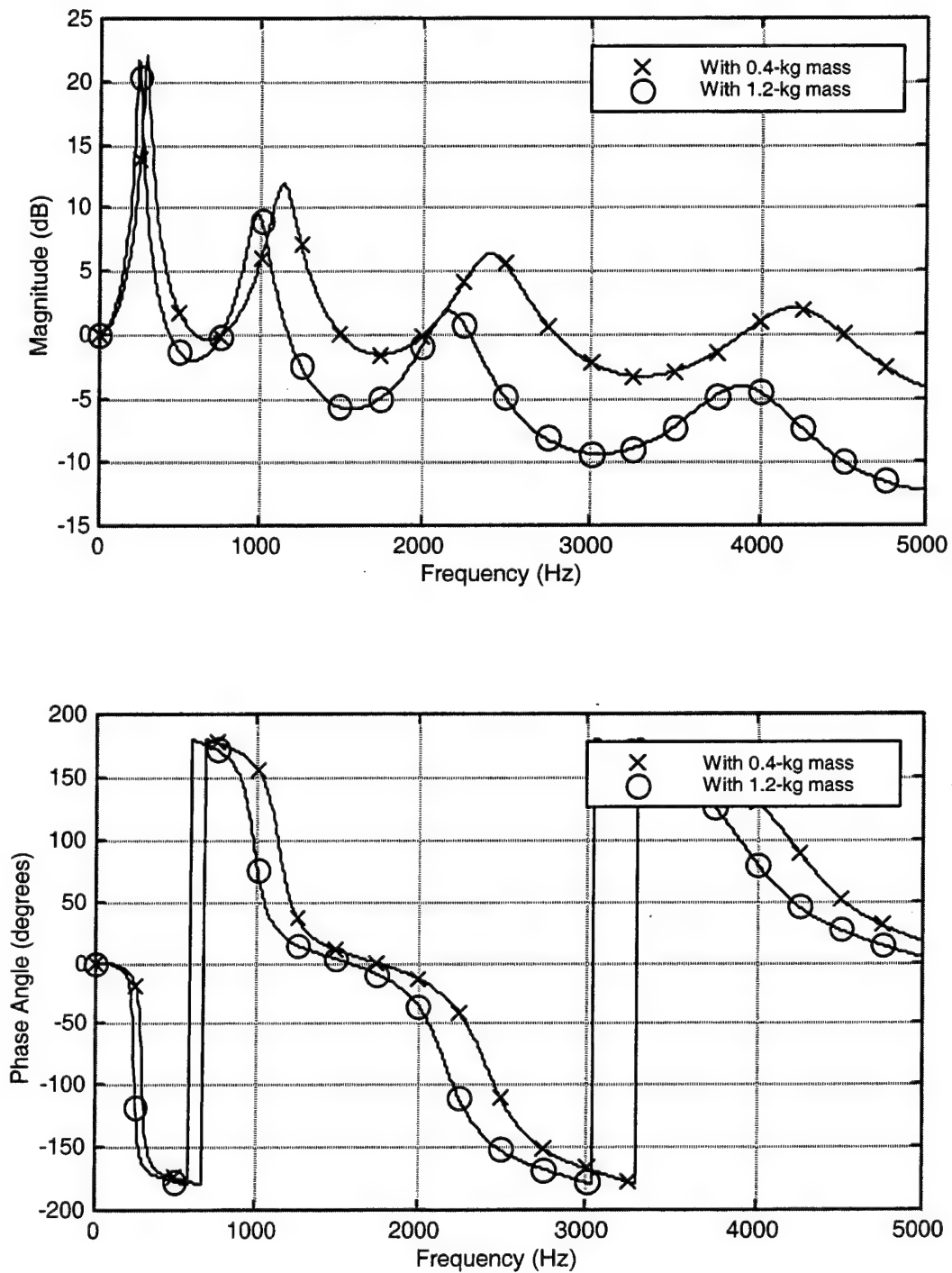
Figure 2, which corresponds to equations (12) and (13), is a plot of magnitude (top) and phase angle (bottom) for the transfer functions  $T_1(\omega)$  and  $T_2(\omega)$  versus frequency. The first transfer function, computed with an attached mass of 0.4 kg, is depicted with x's, and the second, computed with an attached mass of 1.2 kg, is shown with o's.

Figure 3, corresponding to equation (16), is a plot of the function  $s$  versus frequency. Note that although this function is a cosine with respect to frequency, the period is increasing as frequency increases. Table 1 lists the values of  $n$  versus frequency, which were determined by inspection of the figure. Once the values of  $n$  are known, the modulus values of  $E$  can be determined from equations (15)-(18).

Figure 4 shows a plot of real and imaginary Young's modulus values versus frequency. The real (actual) values used to make the transfer functions are displayed as a solid line, and the real (estimated) values are displayed as x's. The imaginary (actual) values used to make the transfer functions are also displayed as a solid line, with the imaginary (estimated) values displayed as o's. The estimated values agree at all frequencies with the actual values. This result is expected because there is no noise in the data and the same parameters used to make the transfer functions are used to calculate the modulus values (i.e., no error is introduced when calculating the modulus from the transfer functions).

Errors, however, are introduced into this method during the measurement of the transfer functions and system parameters. This effect can be simulated by adding noise to the data with random numbers added to the transfer function, as shown in

$$T_e(\omega) = T(\omega) + e\{\text{Re}[T(\omega)]\sigma_a + i\text{Im}[T(\omega)]\sigma_b\} , \quad (19)$$



**Figure 2. Magnitude and Phase Angle for Transfer Functions  $T_1$  and  $T_2$  Versus Frequency**

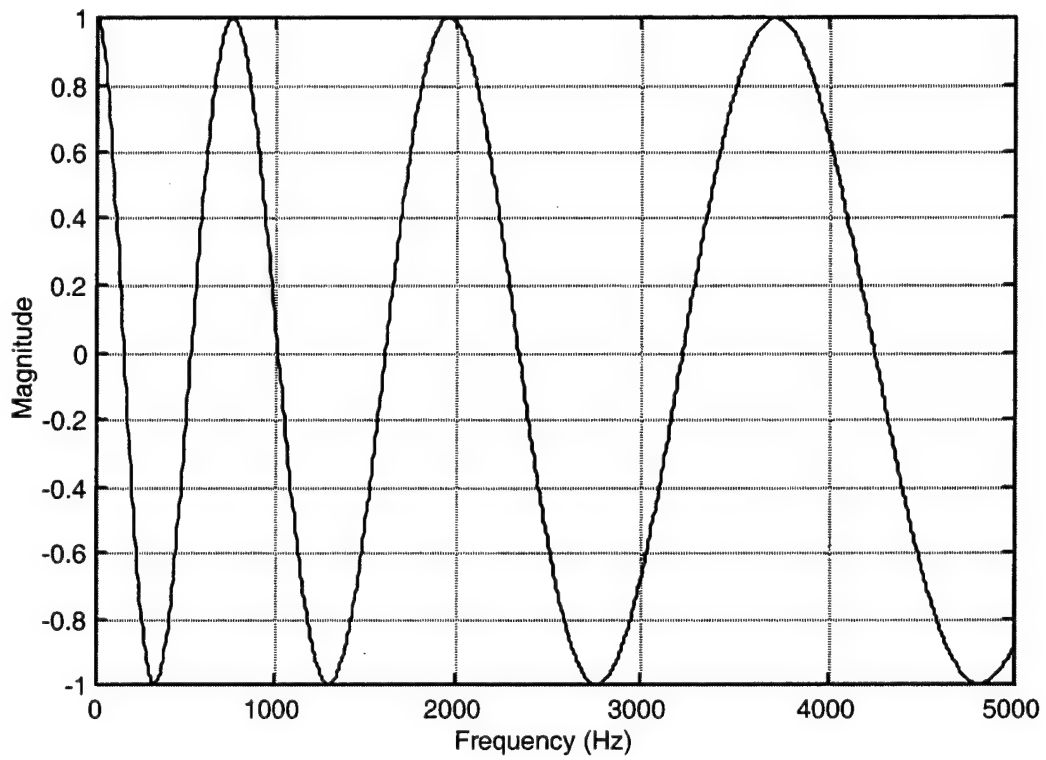


**Figure 3. Function  $s$  Versus Frequency**

**Table 1. Value of  $n$  Versus Frequency**

$n$	Minimum Frequency (Hz)	Maximum Frequency (Hz)
0	0	330
1	330	755
2	755	1295
3	1295	1965
4	1965	2770
5	2770	3715
6	3715	4815
7	4815	5000

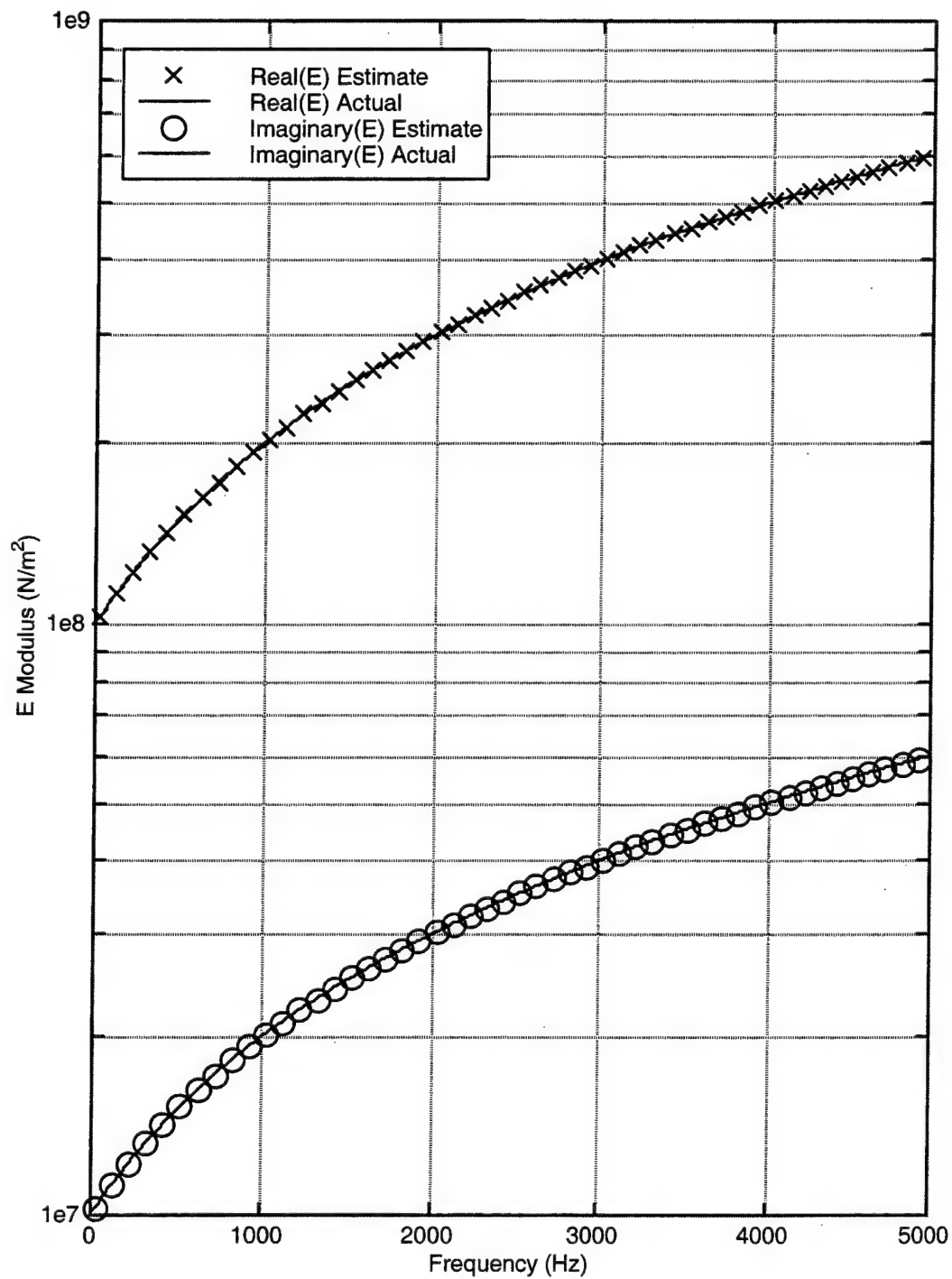


**Figure 4. Real and Imaginary Young's Modulus Values Versus Frequency**



where  $e$  is the amount of error added to the transfer function and where  $\sigma_a$  and  $\sigma_b$  are random numbers with zero mean and a variance of one.

Figure 5, corresponding to equations (12), (13), and (19), is a plot of the transfer functions  $T_1(\omega)$  and  $T_2(\omega)$  with noise versus frequency. The value of  $e$  used to create this figure is 0.03, which represents approximately 3% noise in the data set. (If this test is properly set up and executed, a 3% noise level would be considered even greater than the actual noise levels in the experimental data.)

Figure 6 is a plot of the function  $s$  with and without additive noise versus frequency. The solid line is the function with  $e$  set equal to 0.03, and the o's connected with the dotted line show the function without noise (also seen in figure 3).

Figure 7 plots the estimated and actual values of Young's modulus ( $E$ ) with noise versus frequency. The estimated values of the real part of  $E$  are depicted with x's, and the actual values of the real part of  $E$  are shown as a solid line. The estimated values of the imaginary part of  $E$  are depicted with o's, and the actual values of the imaginary part of  $E$  are shown as a solid line.

The effect of measurement error on the accuracy of the calculation of  $E$  can also be studied with Monte Carlo simulations. Eleven different values of  $e$  were used to build the transfer functions and then calculate the modulus value. Estimation error at each frequency was defined according to

$$\alpha(\omega_m) = \frac{\left| |E_{act}(\omega_m)| - |E_{est}(\omega_m)| \right|}{\max[|E_{act}(\omega_m)|, |E_{est}(\omega_m)|]}, \quad (20)$$

where  $\alpha(\omega_m)$  is Young's modulus estimation error at the  $m$ th frequency, the subscript *act* corresponds to the actual value, and the subscript *est* corresponds to the estimated (calculated) value. Once this value is known, it can be summed across  $M$  frequencies by

$$\beta_j = \frac{1}{M} \sum_{m=1}^M \alpha(\omega_m), \quad (21)$$

where  $\beta_j$  is the average error for the  $j$ th Monte Carlo simulation. Finally, all the simulations can be summed from

$$\varepsilon = \frac{1}{J} \sum_{j=1}^J \beta_j , \quad (22)$$

where  $\varepsilon$  is the estimation error using  $J$  simulations. Table 2 lists transfer function error ( $e$ ) versus Young's modulus estimation error ( $\varepsilon$ ). The frequency range of the values used to prepare this table is 2.5 to 5000 Hz, the number of frequencies ( $M$ ) used to calculate the estimation error is 100, and the number of simulations ( $J$ ) for each value of  $e$  is 100.

Figure 8 is a plot of Young's modulus estimation error ( $\varepsilon$ ) versus frequency for a single simulation ( $J = 1$ ) using a known transfer function error of  $e = 0.03$ . Note that the estimation error for Young's modulus is slightly smaller than the transfer function error in table 2. Also note that the larger estimation errors tend to be near the frequency values where  $n$  is increasing.

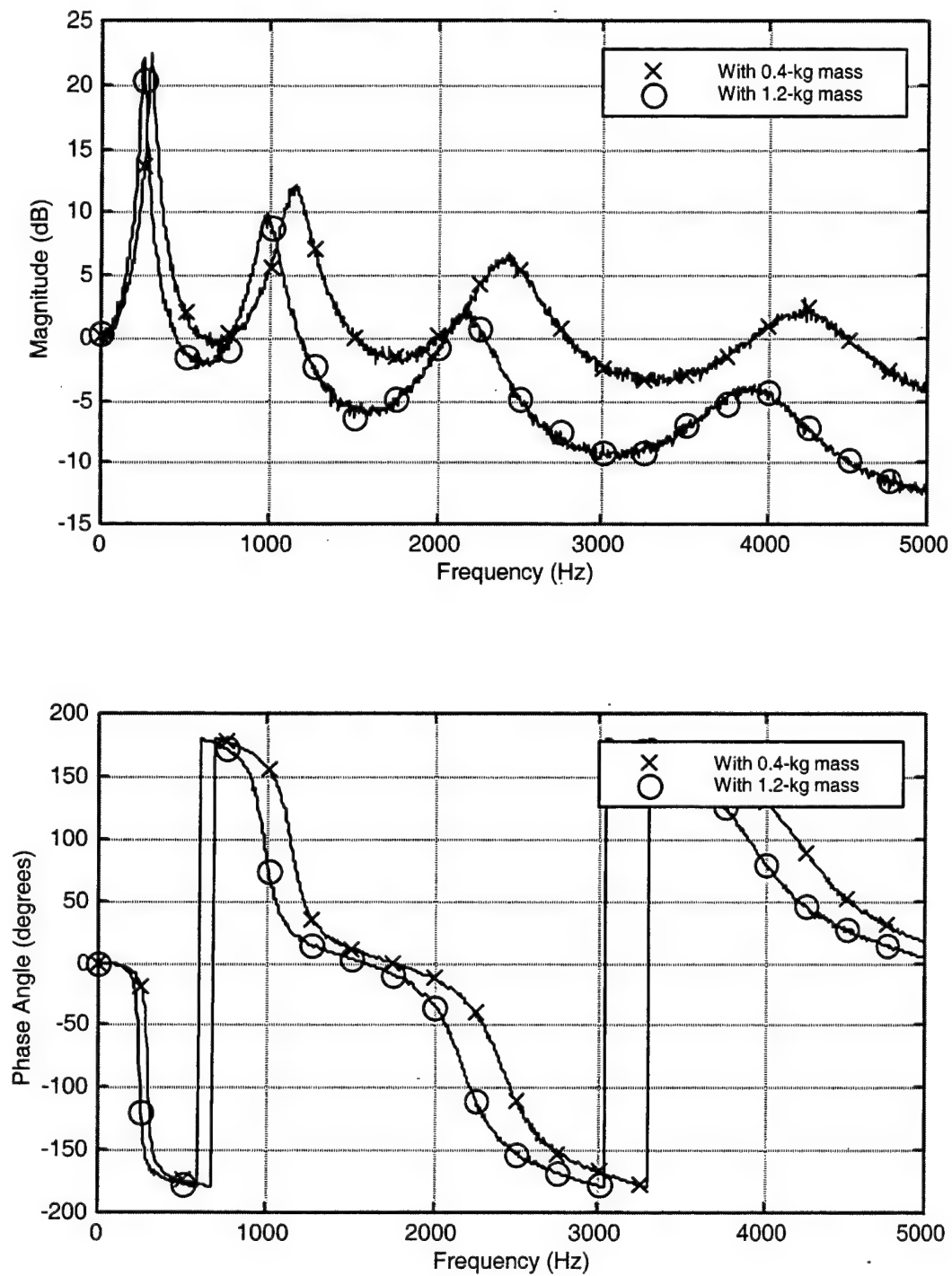


**Figure 5. Magnitude and Phase Angle for Transfer Functions  $T_1$  and  $T_2$  With Noise Versus Frequency**

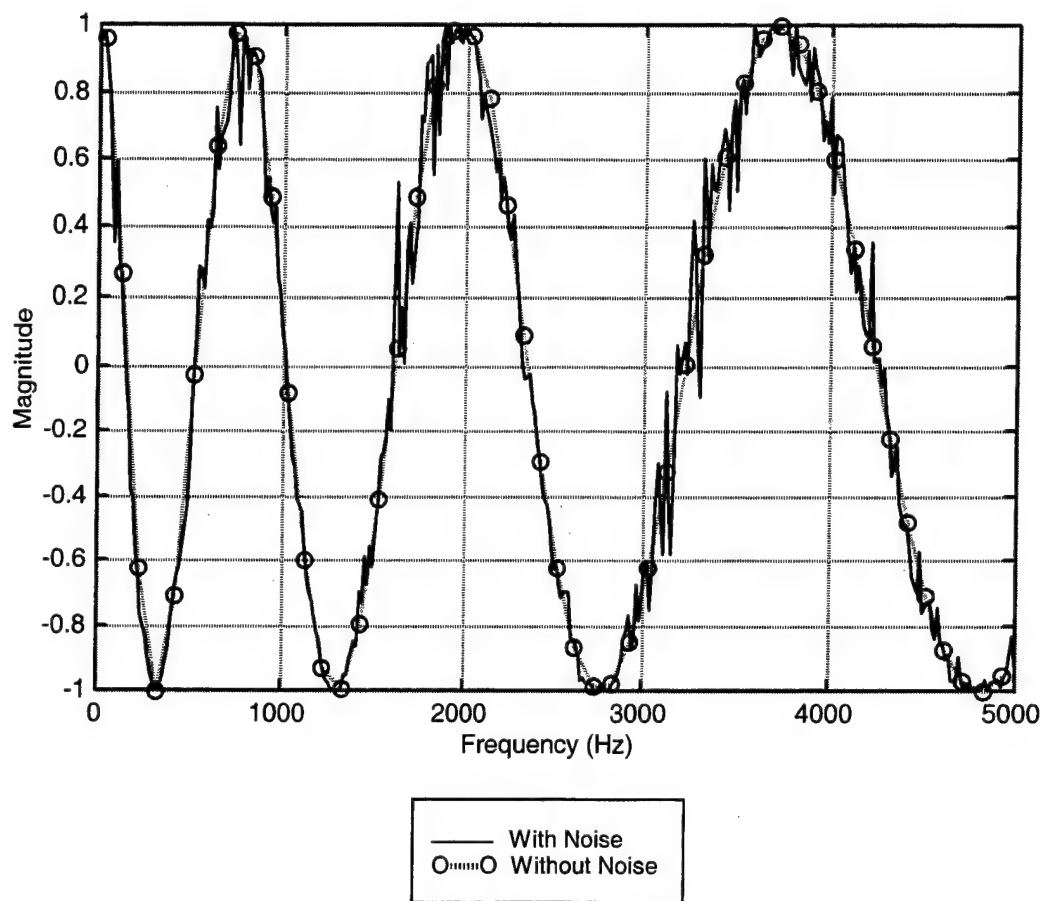


**Figure 6. Function  $s$  With and Without Noise Versus Frequency**

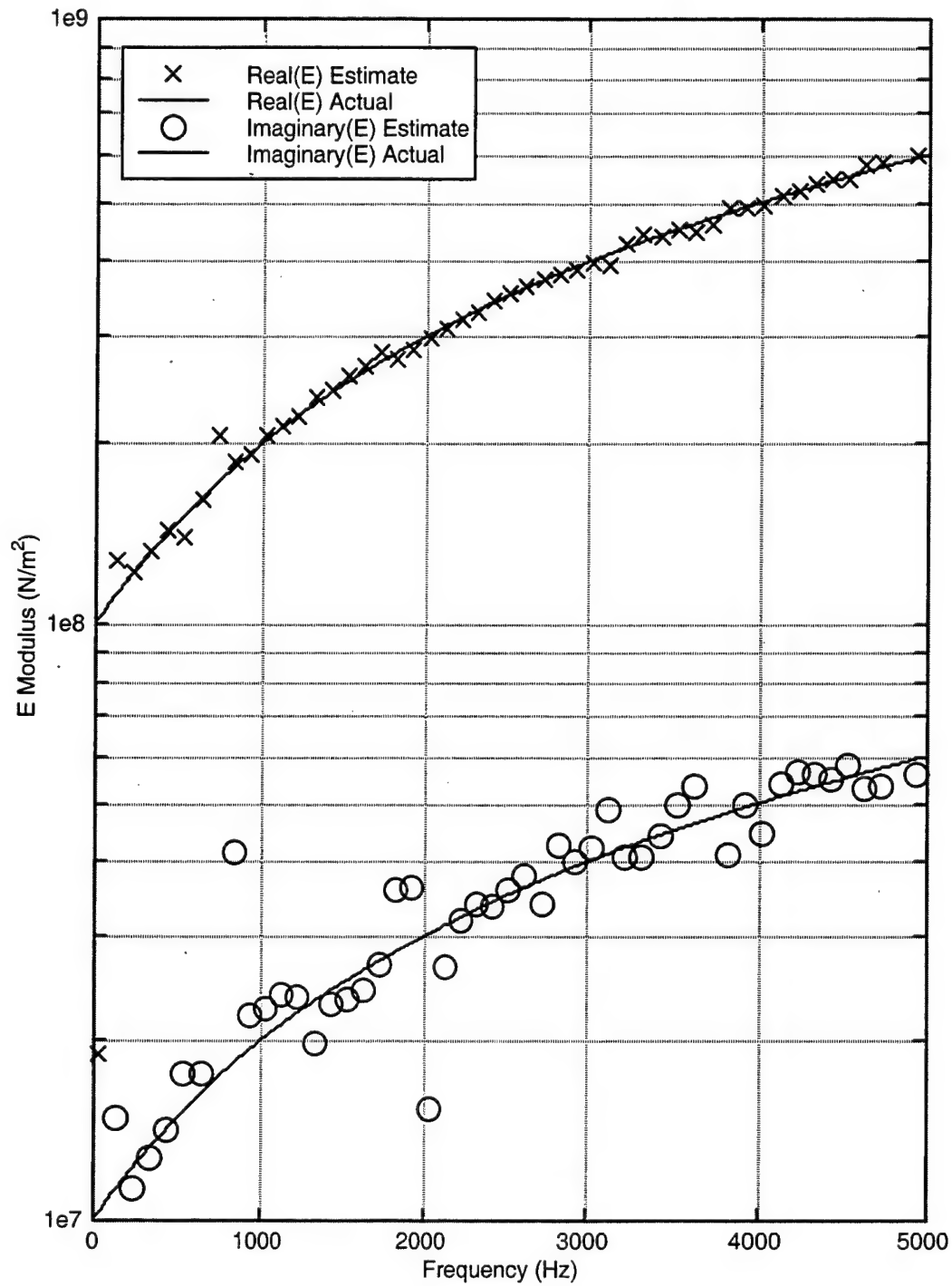


*Figure 7. Real and Imaginary Young's Modulus Values  
Calculated With Noise Versus Frequency*

**Table 2. Transfer Function Error Versus  
Young's Modulus Estimation Error**

<b>Transfer Function Error (<math>e</math>)</b>	<b>Estimation Error (<math>\epsilon</math>)</b>
0	0
0.005	0.004
0.010	0.008
0.015	0.013
0.020	0.019
0.025	0.023
0.030	0.026
0.035	0.031
0.040	0.034
0.045	0.038
0.050	0.041

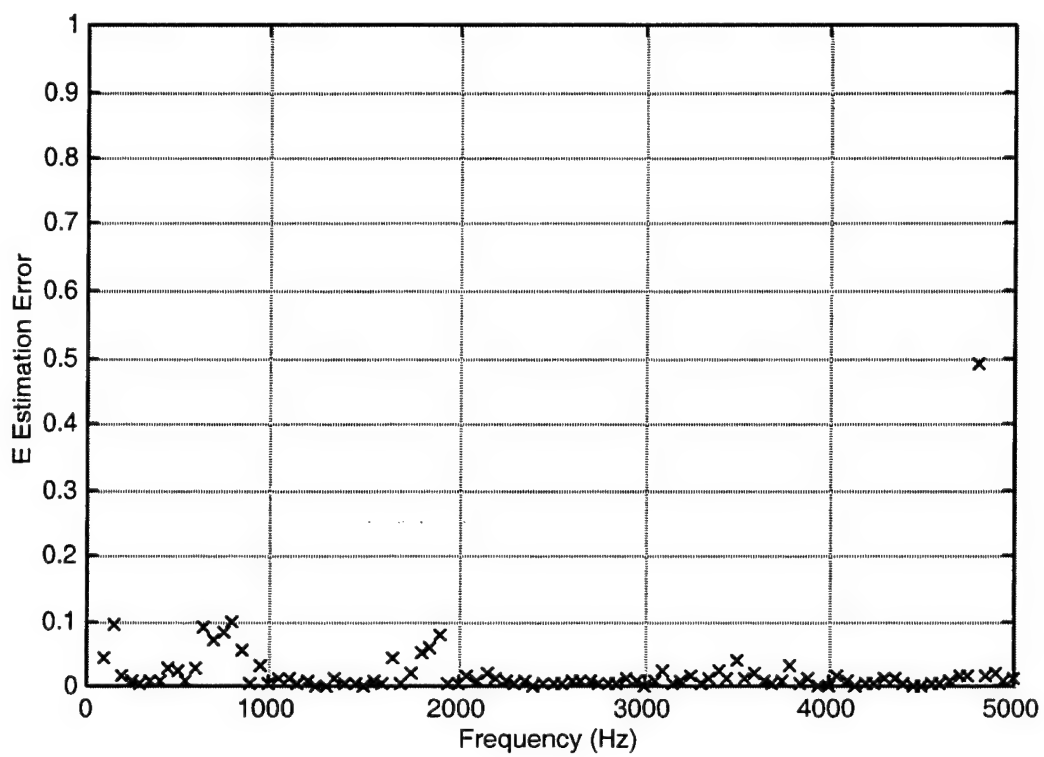


**Figure 8. Young's Modulus Estimation Error ( $\epsilon$ ) Versus Frequency**

#### 4. MEASUREMENT OF SHEAR MODULUS

Measuring the shear modulus of the cylindrical test specimen\* requires mounting the shaker longitudinally to a stiff connecting rod (not to the specimen), which is connected to the edge of a large disk. A bearing mounted at the center of the disk allows it to rotate freely about its center point. The test specimen is rigidly attached to the middle of this disk in such a manner that when the disk is pushed by the connecting rod, it initiates torsional (or rotational) response in the specimen. The other end of the test specimen is attached to a second disk that provides rotary inertia when the test is run. Two accelerometers are used – one attached to the first disk and one attached to the second disk – with the measurement axis of both in the same angular direction as the disks. Although each accelerometer measures translation, this value can be converted into angular rotation by multiplying the recorded value by the distance from the center of the disk to the accelerometer. The laboratory configuration for this experiment is shown in figure 9.

As can be seen in the figure, the shaker inputs energy into the connecting rod in the form of linear translation. When the rod inputs the energy into the disk, the disk rotates and initiates a shear wave in the test specimen. The speed and loss of this wave can be measured with the two accelerometers, and the shear modulus can be calculated from the result. This measurement (estimation) process, which is extremely similar to the measurement of Young's modulus, is described below.

The system model represents a cylindrical test specimen (bar) attached via a disk and connecting rod to a torsional shaker at  $x = 0$  and to a disk with rotary inertia at  $x = L$ . Each disk has an accelerometer to measure the angular acceleration levels at its end. The linear second-order wave equation modeling angular rotation in the bar is

$$\frac{\partial^2 \theta(x,t)}{\partial t^2} - \frac{G}{\rho} \frac{\partial^2 \theta(x,t)}{\partial x^2} = 0, \quad (23)$$

---

\*As with Young's modulus, two sets of experimental measurements are recorded, with the disk (at  $x = L$ ) in the second set having a different rotary inertial value than the one in the first set.



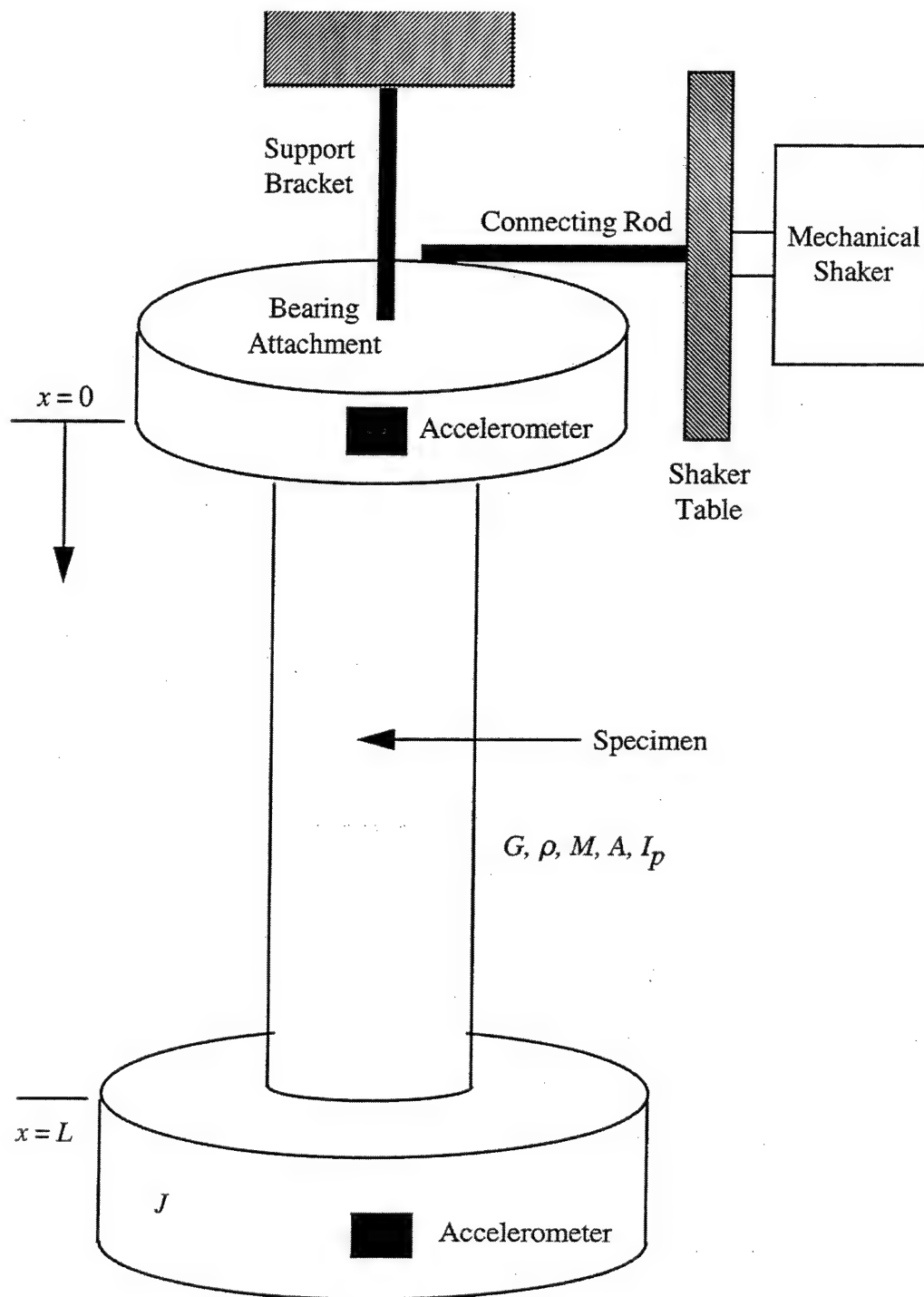


*Figure 9. Laboratory Configuration for Measuring Shear Modulus*

where  $\theta(x,t)$  is the angular rotation at location  $x$  (m) and time  $t$  (s),  $\rho$  is the density of the bar ( $\text{kg/m}^3$ ), and  $G$  is the unknown, frequency-dependent, complex shear modulus of elasticity ( $\text{N/m}^2$ ), which is yet to be determined. The boundary at  $x = 0$  is modeled as a fixed end with harmonic angular motion and is expressed as

$$\theta(0,t) = \Theta_0 \exp(i\omega t) , \quad (24)$$

where  $\omega$  is the frequency of excitation (rad/s),  $\Theta_0$  is the amplitude (rad), and  $i$  is the square root of -1. The boundary at  $x = L$  is formulated by matching the angular force (torque) at the end of the bar to the rotary inertia of the end mass multiplied by its angular acceleration and is expressed as

$$GI_p \frac{\partial \theta(L,t)}{\partial x} = -J \frac{\partial^2 \theta(L,t)}{\partial t^2} , \quad (25)$$

where  $I_p$  is the polar moment of inertia in the cross-section of the bar ( $\text{m}^4$ ) and  $J$  is the rotary inertia of the disk at the end of the bar ( $\text{kg}\cdot\text{m}^2$ ). For the cylindrical test specimen, the polar moment of inertia is

$$I_p = \frac{\pi}{2} a^4 , \quad (26)$$

where  $a$  is the radius of the specimen (m). For a cylindrical disk, the rotary inertia is

$$J = \frac{1}{2} m r^2 , \quad (27)$$

where  $r$  is the radius of the disk (m) and  $m$  is the mass of the disk (kg).

Equation (23) can be rewritten in the spatial domain as

$$\frac{d^2\Theta(x,\omega)}{dx^2} + k_G^2\Theta(x,\omega) = 0 , \quad (28)$$

where  $\Theta(x,\omega)$  is the temporal Fourier transform of the axial displacement and  $k_G$  is the complex shear wavenumber (rad/m), which is equal to

$$k_G = \omega / \sqrt{G/\rho} . \quad (29)$$

Similarly, equation (24) becomes

$$\Theta(0,\omega) = \Theta_0 , \quad (30)$$

and equation (25) becomes

$$GI_p \frac{d\Theta(L,\omega)}{dx} = J\omega^2\Theta(L,\omega) . \quad (31)$$

The solution to equation (28) is

$$\Theta(x,\omega) = X(\omega)\cos(k_G x) + Z(\omega)\sin(k_G x) , \quad (32)$$

where  $X$  and  $Z$  are wave propagation constants. Applying boundary conditions (30) and (31) to equation (32) — and writing the solution as a transfer function in the form of a ratio between the rotation at both ends — produces

$$\frac{\Theta(L,\omega)}{\Theta_0} = \left[ \frac{1}{\cos(k_G L) - \lambda(k_G L)\sin(k_G L)} \right] , \quad (33)$$

where  $\lambda$  is equal to

$$\lambda = \frac{2J}{a^2 M}, \quad (34)$$

and  $M$  is the mass of the bar (kg) expressed as

$$M = \rho AL. \quad (35)$$

The transfer function in equation (33) represents experimental data and is a function of unknown wavenumber  $k_G$ . The inversion of the two transfer functions obtained from the different attached rotary inertial masses will allow both sets of data to be combined, yielding a closed-form solution of  $k_G$  and then  $G$  as a function of  $\omega$ . The theoretical forms of these transfer functions are

$$\frac{\Theta(L, \omega)}{\Theta_0} = S_1(\omega) = \left[ \frac{1}{\cos(k_G L) - \lambda_1(k_G L) \sin(k_G L)} \right] \quad (36)$$

and

$$\frac{\Theta(L, \omega)}{\Theta_0} = S_2(\omega) = \left[ \frac{1}{\cos(k_G L) - \lambda_2(k_G L) \sin(k_G L)} \right], \quad (37)$$

where the subscript 1 denotes the first attached rotary inertial mass and the subscript 2 denotes the second attached rotary inertial mass. Although the theoretical forms given in equations (36) and (37) are end rotation divided by input rotation, the transfer function created by end rotational acceleration divided by input rotational acceleration (which is obtained from the accelerometers) is identical in the frequency domain. Writing equations (36) and (37) as a function of  $(k_G L) \sin(k_G L)$  and then equating them yields

$$\cos(k_G L) = \frac{S_2 \lambda_2 - S_1 \lambda_1}{S_1 S_2 (\lambda_2 - \lambda_1)} = \varphi, \quad (38)$$

where  $\varphi$  is a complex quantity. The inversion of equation (38) allows the complex wavenumber to be solved as a function of  $\varphi$ . This solution to the real part of  $k_G$  is

$$\text{Re}(k_G) = \begin{cases} \frac{1}{2L} \text{Arccos}(r) + \frac{m\pi}{2L} & m \text{ even} \\ \frac{1}{2L} \text{Arccos}(-r) + \frac{m\pi}{2L} & m \text{ odd} \end{cases}, \quad (39)$$

where

$$r = [\text{Re}(\varphi)]^2 + [\text{Im}(\varphi)]^2 - \sqrt{[\text{Re}(\varphi)]^2 + [\text{Im}(\varphi)]^2}^2 - \{2[\text{Re}(\varphi)]^2 - 2[\text{Im}(\varphi)]^2 - 1\}, \quad (40)$$

$m$  is a non-negative integer, and capital A denotes the principal value of the inverse cosine function. The value of  $m$  is determined from the function  $r$ , which is a cosine function with respect to frequency. At zero frequency,  $m$  is 0. Every time  $s$  cycles through  $\pi$  radians ( $180^\circ$ ),  $m$  is increased by 1. After the solution to the real part of  $k_G$  is found, the solution to its imaginary part is written as

$$\text{Im}(k_G) = \frac{1}{L} \log_e \left\{ \frac{\text{Re}(\varphi)}{\cos[\text{Re}(k_G)L]} - \frac{\text{Im}(\varphi)}{\sin[\text{Re}(k_G)L]} \right\}. \quad (41)$$

Once the real and imaginary parts of wavenumber  $k_G$  are known, the complex-valued modulus of elasticity can be determined at each frequency with

$$G(\omega) = \text{Re}[G(\omega)] + i \text{Im}[G(\omega)] = \frac{\rho \omega^2}{[\text{Re}(k_G) + i \text{Im}(k_G)]^2}. \quad (42)$$

Equations (23)-(42) produce an estimate of shear modulus at every frequency for which a measurement is made.

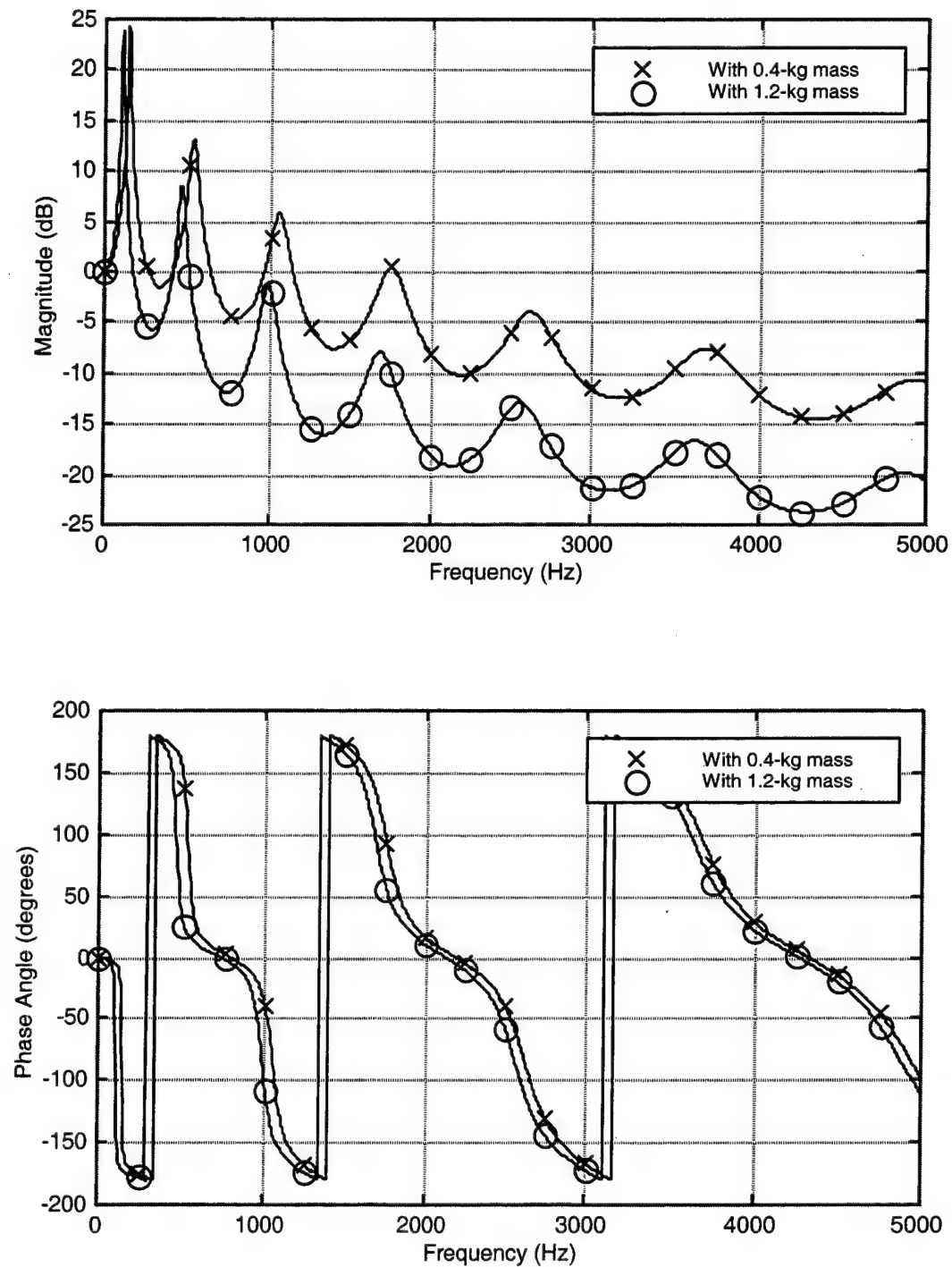
## 5. NUMERICAL SIMULATION OF SHEAR MODULUS MEASUREMENT

Numerical simulations conducted to determine the effectiveness of this method use the same parameters to define a baseline problem as in section 3:  $M = 4.0$  kg,  $m_1 = 0.4$  kg,  $m_2 = 1.2$  kg,  $L = 0.254$  m,  $\rho = 1200$  kg/m<sup>3</sup>,  $\text{Re}(E) = 10^8 + 10^5 f$  N/m<sup>2</sup>, and  $\text{Im}(E) = 10^7 + 10^4 f$  N/m<sup>2</sup>, where  $f$  is frequency in Hertz. The one additional parameter required is the radius of the rotary inertial masses, which is chosen to be 0.1016 m. From the above baseline values, the rotary inertial values of the masses are calculated to be  $J_1 = 0.0021$  kg•m<sup>2</sup> and  $J_2 = 0.0062$  kg•m<sup>2</sup>, which are used to compute the ratios  $\lambda_1$  and  $\lambda_2$  as 0.247 and 0.741, respectively. The shear modulus values in this analysis are  $\text{Re}(G) = 3.58 \times 10^7 + 3.43 \times 10^4 f$  N/m<sup>2</sup> and  $\text{Im}(E) = 2.55 \times 10^6 + 2.34 \times 10^3 f$  N/m<sup>2</sup>, where  $f$  is frequency in Hertz.

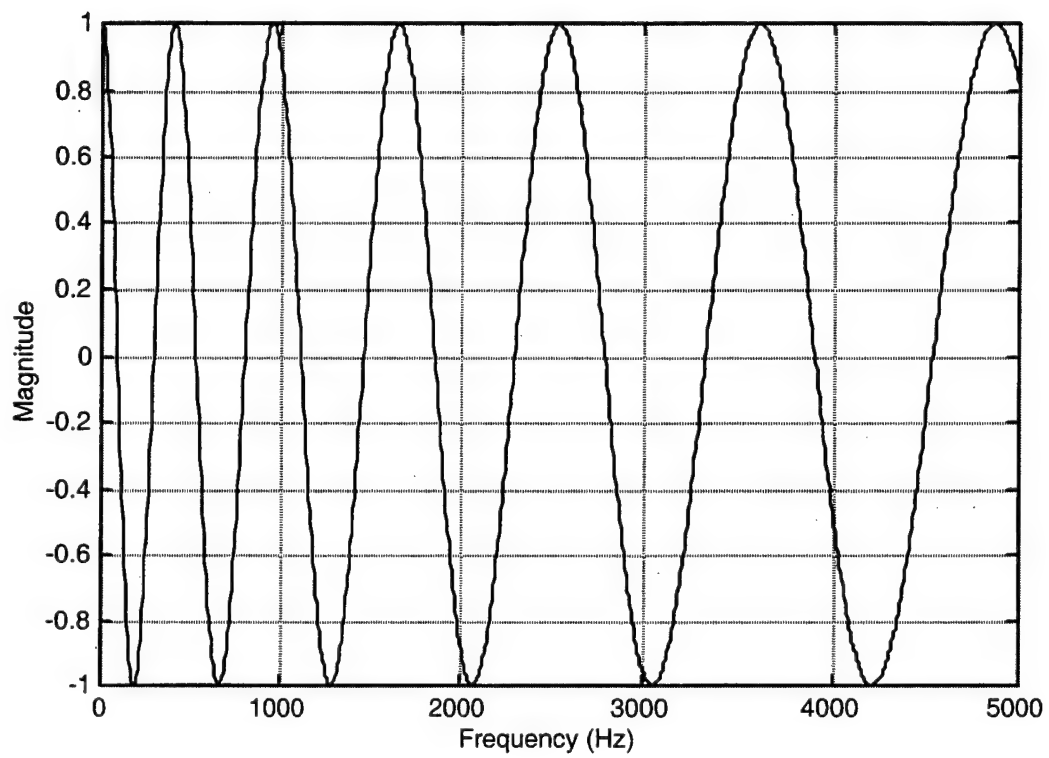
Figure 10, corresponding to equations (36) and (37), shows the transfer functions  $S_1(\omega)$  and  $S_2(\omega)$  versus frequency for magnitude (top plot) and phase angle (bottom plot). The first transfer function was computed with an attached mass of 0.4 kg and is depicted with x's; the second transfer function was computed with an attached mass of 1.2 kg and is shown with o's.

Figure 11 corresponds to equation (40) and is a plot of the function  $r$  versus frequency. Note that although this function is a cosine with respect to frequency, the period is increasing as frequency increases. Table 3 provides a list of the values of  $m$  versus frequency, which were determined by inspection of this figure. Once the values of  $m$  are known, the modulus values of  $G$  can be determined from equations (23)-(42).

Figure 12 is a plot of real and imaginary shear modulus values versus frequency. The real (actual) values used to make the transfer functions are displayed as a solid line, and the real (estimated) values are displayed as x's. The imaginary (actual) values used to make the transfer functions are also displayed as a solid line, with the imaginary (estimated) values displayed as o's. The estimated values agree at all frequencies with the actual values. This result is expected because there is no noise in the data and the same parameters used to make the transfer functions are also used to calculate the modulus values (i.e., no error is introduced when calculating the modulus from the transfer functions).



**Figure 10. Magnitude and Phase Angle for Transfer Functions  $S_1$  and  $S_2$  Versus Frequency**



**Figure 11. Function  $r$  Versus Frequency**



**Table 3. Value of  $m$  Versus Frequency**

<b><math>m</math></b>	<b>Minimum Frequency (Hz)</b>	<b>Maximum Frequency (Hz)</b>
0	0	185
1	185	405
2	405	655
3	655	945
4	945	1280
5	1280	1655
6	1655	2075
7	2075	2540
8	2540	3050
9	3050	3610
10	3610	4215
11	4215	4865
12	4865	5000

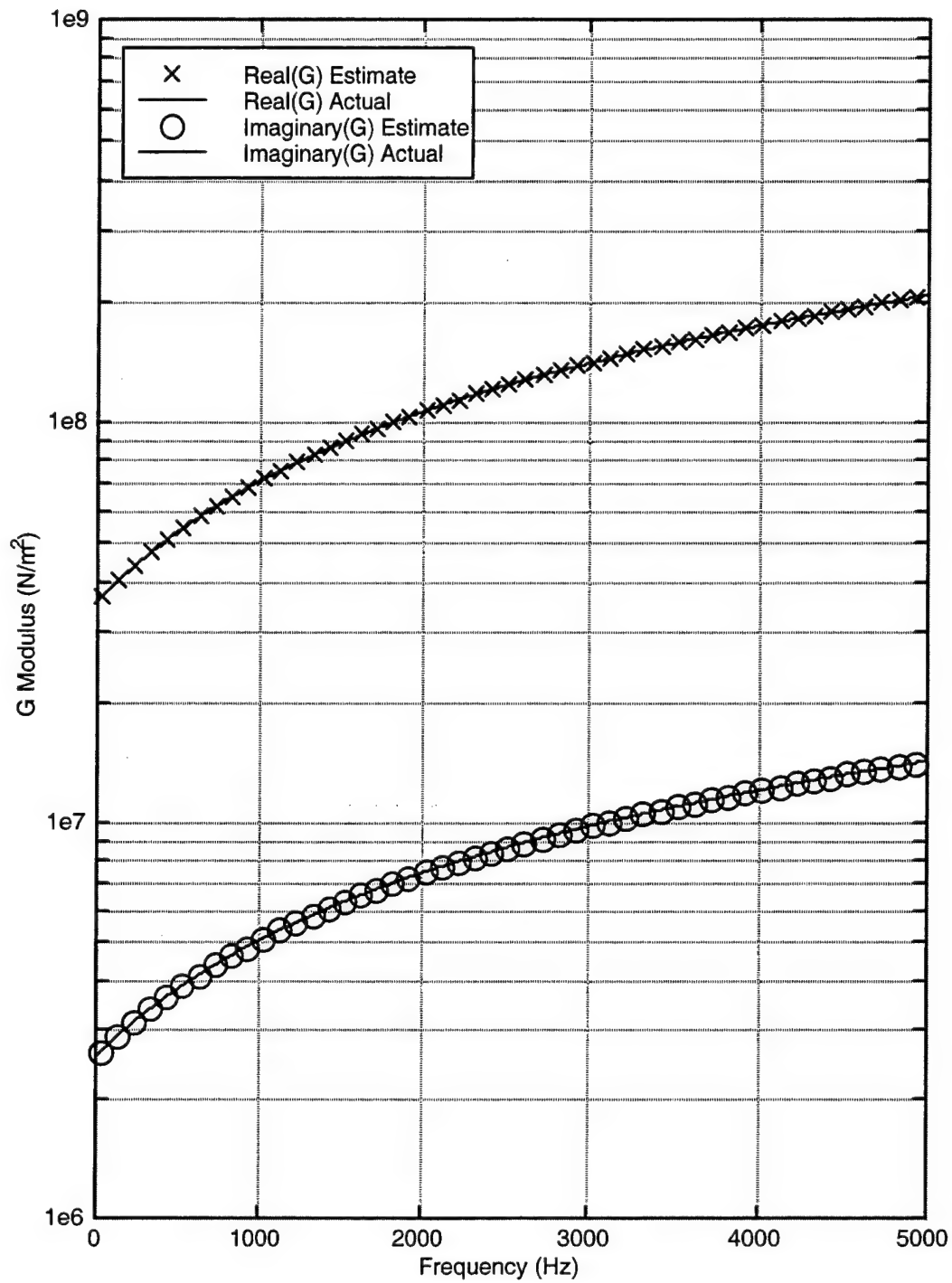


**Figure 12. Real and Imaginary Shear Modulus Values Versus Frequency**

Errors, however, are introduced into this method during the measurement of the transfer functions and system parameters. This effect can be simulated by adding noise to the data using random numbers added to the transfer function, as shown by

$$S_e(\omega) = S(\omega) + e\{\text{Re}[S(\omega)]\sigma_a + i\text{Im}[S(\omega)]\sigma_b\} , \quad (43)$$

where  $e$  is the amount of error added to the transfer function and where  $\sigma_a$  and  $\sigma_b$  are random numbers with zero mean and a variance of one.

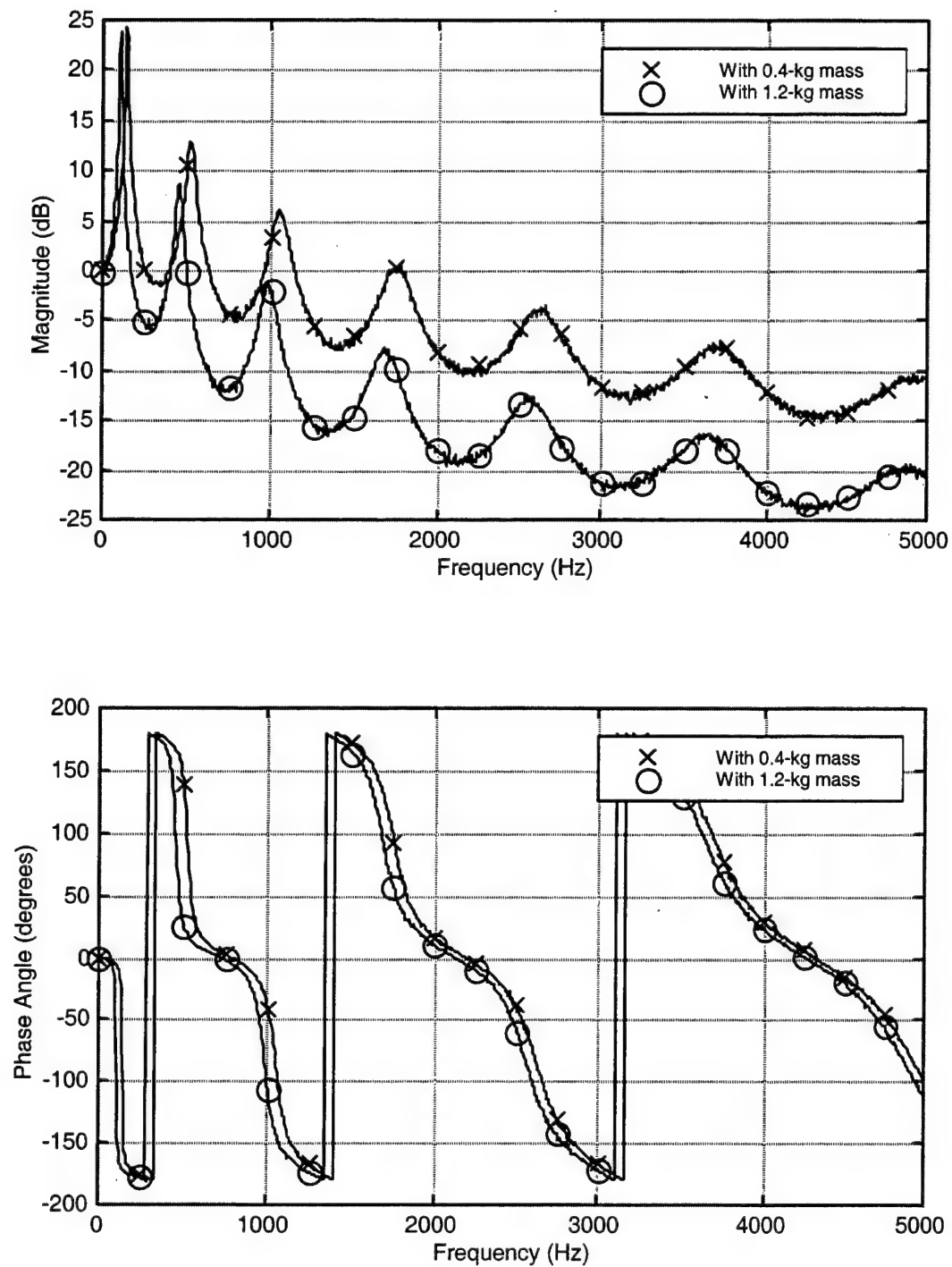
Figure 13, corresponding to equations (36), (37), and (43), is a plot of the transfer functions  $S_1(\omega)$  and  $S_2(\omega)$  with noise versus frequency. The value of  $e$  used to create this figure is 0.03, which represents roughly 3% noise in the data set. (If this test is properly set up and executed, a 3% noise level would be considered greater than the actual noise levels in the experimental data.)

Figure 14 is a plot of the function  $r$  with and without additive noise versus frequency. The solid line is the function with  $e$  set equal to 0.03, and the o's connected with the dotted line show the function without noise (also seen in figure 11).

Figure 15 is a plot of the estimated and actual values of the shear modulus ( $G$ ) versus frequency. The estimated values of the real part of  $G$  are depicted with x's, and the actual values of the real part of  $G$  are shown as a solid line. The estimated values of the imaginary part of  $G$  are depicted with o's, and the actual values of the imaginary part of  $G$  are shown as a solid line.

The effect of the measurement error on the accuracy of the calculation of  $G$  can also be studied with Monte Carlo simulations. Eleven different values of  $e$  were used to build the transfer functions and then calculate the modulus value. Estimation error at each frequency was defined according to

$$\alpha(\omega_m) = \frac{\left| |G_{act}(\omega_m)| - |G_{est}(\omega_m)| \right|}{\max[|G_{act}(\omega_m)|, |G_{est}(\omega_m)|]} , \quad (44)$$



**Figure 13. Magnitude and Phase Angle for Transfer Functions  $S_1$  and  $S_2$  With Noise Versus Frequency**

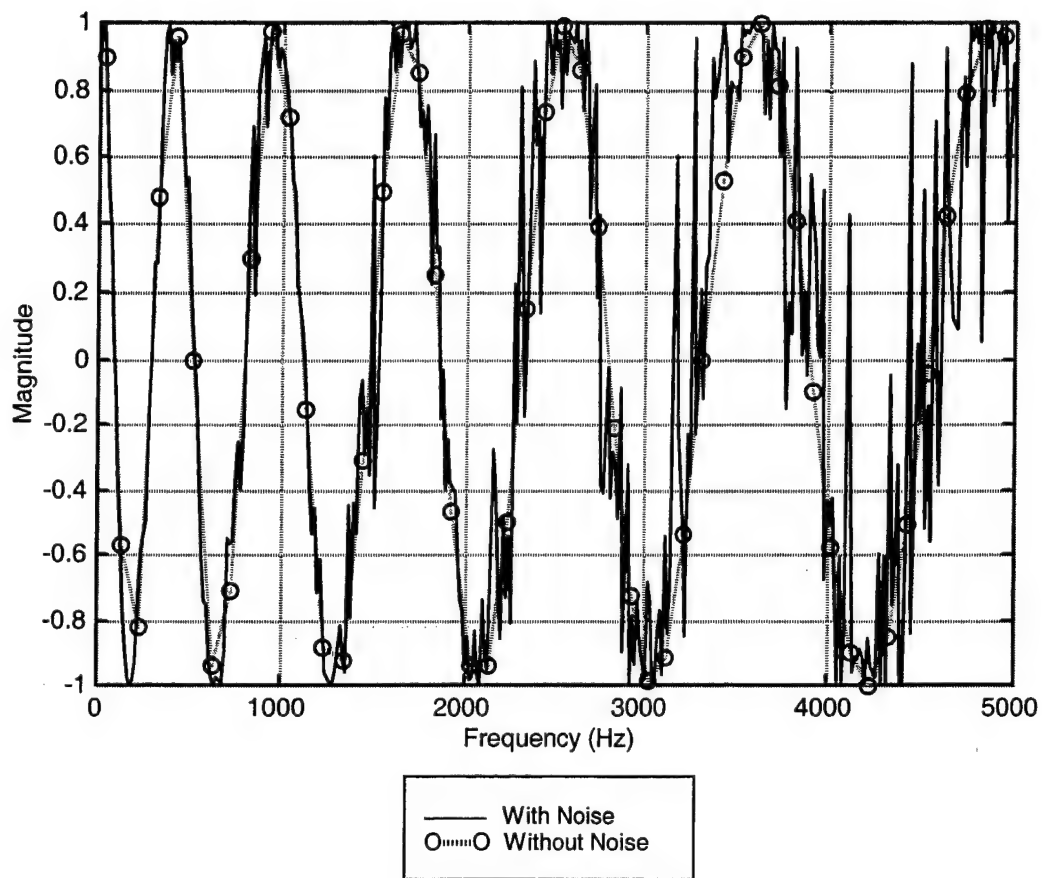


**Figure 14. Function  $r$  With and Without Noise Versus Frequency**

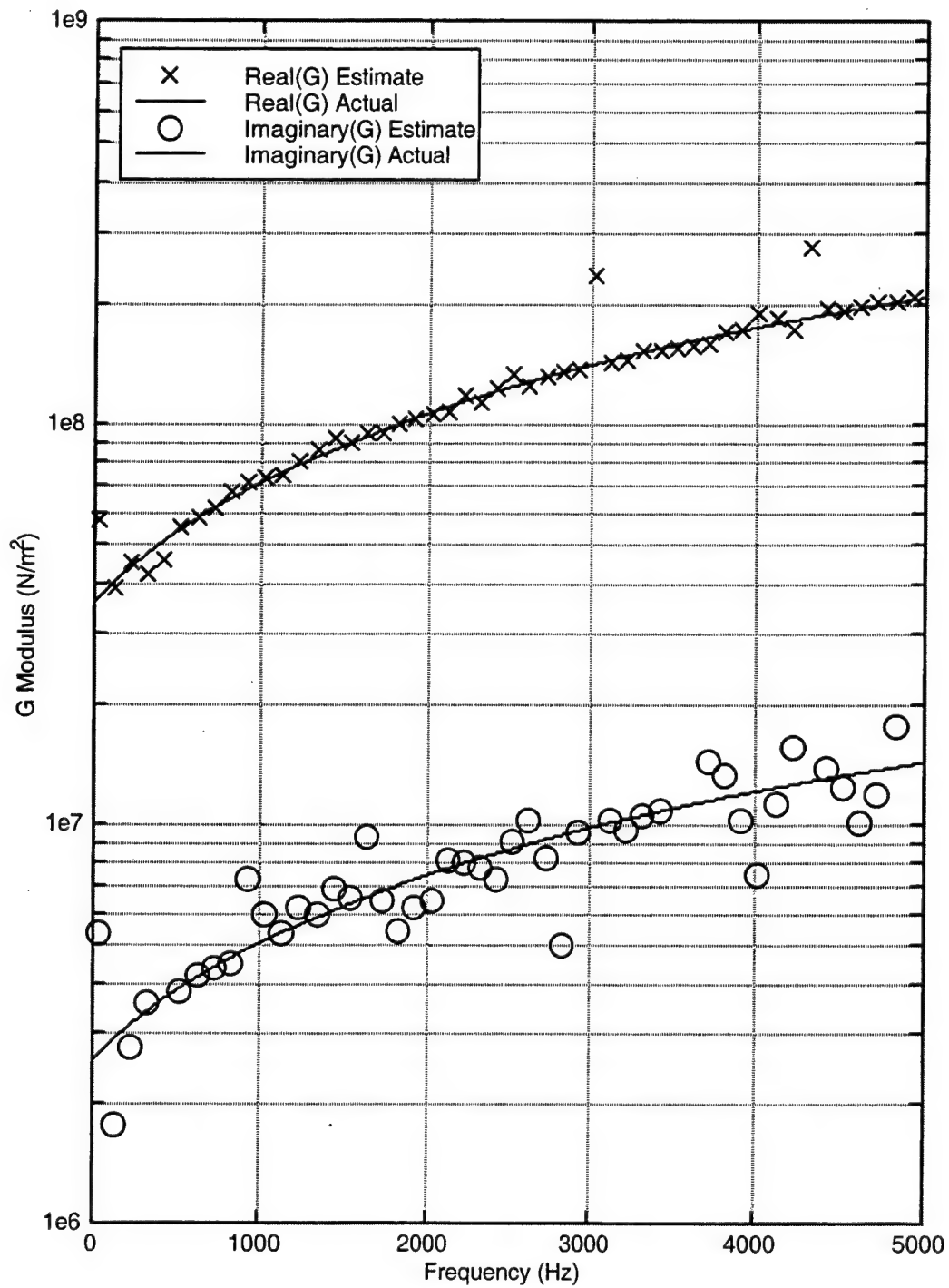


**Figure 15. Real and Imaginary Shear Modulus Values  
Calculated with Noise Versus Frequency**

where  $\alpha(\omega_m)$  is the shear modulus estimation error at the  $m$ th frequency, the subscript *act* corresponds to the actual value, and the subscript *est* corresponds to the estimated (calculated) value. Once this value is known, it can be summed across  $M$  frequencies by

$$\beta_j = \frac{1}{M} \sum_{m=1}^M \alpha(\omega_m) , \quad (45)$$

where  $\beta_j$  is the average error for the  $j$ th Monte Carlo simulation. Finally, all the simulations can be summed from

$$\varepsilon = \frac{1}{J} \sum_{j=1}^J \beta_j , \quad (46)$$

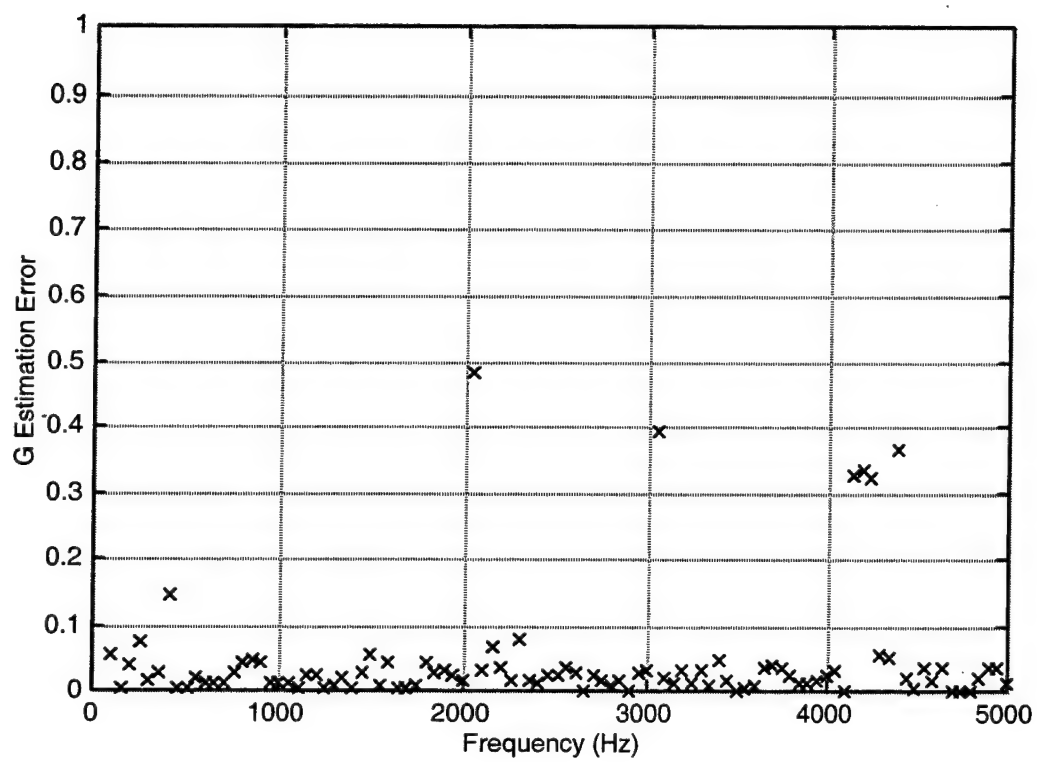
where  $\varepsilon$  is the estimation error using  $J$  simulations. Table 4 lists transfer function error ( $e$ ) versus shear modulus estimation error ( $\varepsilon$ ). The frequency range of the values used to prepare this table is 2.5 to 5000 Hz; the number of frequencies ( $M$ ) used to calculate the estimation error is 100; and the number of simulations ( $J$ ) for each value of  $e$  is 100.

Figure 16 is a plot of shear modulus estimation error ( $\varepsilon$ ) versus frequency for a single simulation ( $J = 1$ ) using a known transfer function error of  $e = 0.03$ . Note that the estimation error for the shear modulus is slightly larger than the transfer function error in table 4. Also note that the larger estimation errors tend to be near the frequency values where  $m$  is increasing.

**Table 4. Transfer Function Error Versus Shear Modulus Estimation Error**

<b>Transfer Function Error (<math>e</math>)</b>	<b>Estimation Error (<math>\epsilon</math>)</b>
0	0
0.005	0.007
0.010	0.013
0.015	0.020
0.020	0.028
0.025	0.035
0.030	0.041
0.035	0.048
0.040	0.052
0.045	0.058
0.050	0.062





**Figure 16. Shear Modulus Estimation Error ( $\epsilon$ ) Versus Frequency**

## 6. MEASUREMENT OF POISSON'S RATIO

The estimation of Poisson's ratio is achieved by combining the Young's modulus and shear modulus previously measured. This equation is expressed as

$$v = \left[ \frac{E}{2G} \right] - 1, \quad (47)$$

where  $v$  is Poisson's ratio and is dimensionless. The formulation in this method allows for Poisson's ratio to be a complex number, although typically the imaginary part of this number is very small or zero.

Figure 17 is a plot of the estimated and actual values of Poisson's ratio versus frequency for a simulation with no noise. The estimated values of the real part of Poisson's ratio are depicted with x's, and the actual values of the real part of Poisson's ratio are shown as a solid line. The estimated values of the imaginary part of Poisson's ratio are depicted with o's, and the actual values of the imaginary part of Poisson's ratio are shown as a solid line. The estimated values agree at all frequencies with the actual values, which is expected because there is no noise in the data and the same parameters used to make the transfer functions are used to calculate the moduli values (i.e., no error is introduced when calculating the moduli from the transfer functions).

Figure 18 is a plot of the estimated and actual values of Poisson's ratio versus frequency with noise simulated using error  $e = 0.03$ . The estimated values of the real part of Poisson's ratio are depicted with x's, and the actual values of the real part of Poisson's ratio are shown as a solid line. The estimated values of the imaginary part of Poisson's ratio are depicted with o's, and the actual values of the imaginary part of Poisson's ratio are shown as a solid line.

The effect of measurement error on the accuracy of the calculation of  $v$  can be studied with Monte Carlo simulations. Eleven different values of  $e$  were used to build the transfer functions and then calculate the Poisson's ratio. The estimation error at each frequency was defined using the equation

$$\alpha(\omega_m) = \frac{\left| |v_{act}(\omega_m)| - |v_{est}(\omega_m)| \right|}{\max[v_{act}(\omega_m), v_{est}(\omega_m)]}, \quad (48)$$

where  $\alpha(\omega_m)$  is the Poisson's ratio estimation error at the  $m$ th frequency, the subscript *act* corresponds to the actual value, and the subscript *est* corresponds to the estimated (calculated) value. Once this value of  $\alpha$  is known, it can be summed across  $M$  frequencies by

$$\beta_j = \frac{1}{M} \sum_{m=1}^M \alpha(\omega_m), \quad (49)$$

where  $\beta_j$  is the average error for the  $j$ th Monte Carlo simulation. Finally, all the simulations can be summed from

$$\varepsilon = \frac{1}{J} \sum_{j=1}^J \beta_j, \quad (50)$$

where  $\varepsilon$  is the estimation error using  $J$  simulations. Table 5 lists transfer function error ( $e$ ) versus Poisson's ratio estimation error ( $\varepsilon$ ). The frequency range of the values used to prepare this table is 2.5 to 5000 Hz; the number of frequencies ( $M$ ) used to calculate the estimation error is 100; and the number of simulations ( $J$ ) for each value of  $e$  is 100.

Figure 19 is a plot of Poisson's ratio estimation error ( $\varepsilon$ ) versus frequency for a single simulation ( $J = 1$ ) using a known transfer function error of  $e = 0.03$ . The estimation error, while small, is not as small as the estimation error found in the calculation of Young's and shear moduli. This result is expected because the errors from both the estimation of Young's modulus and shear modulus are contributing to the error in the estimation of Poisson's ratio.

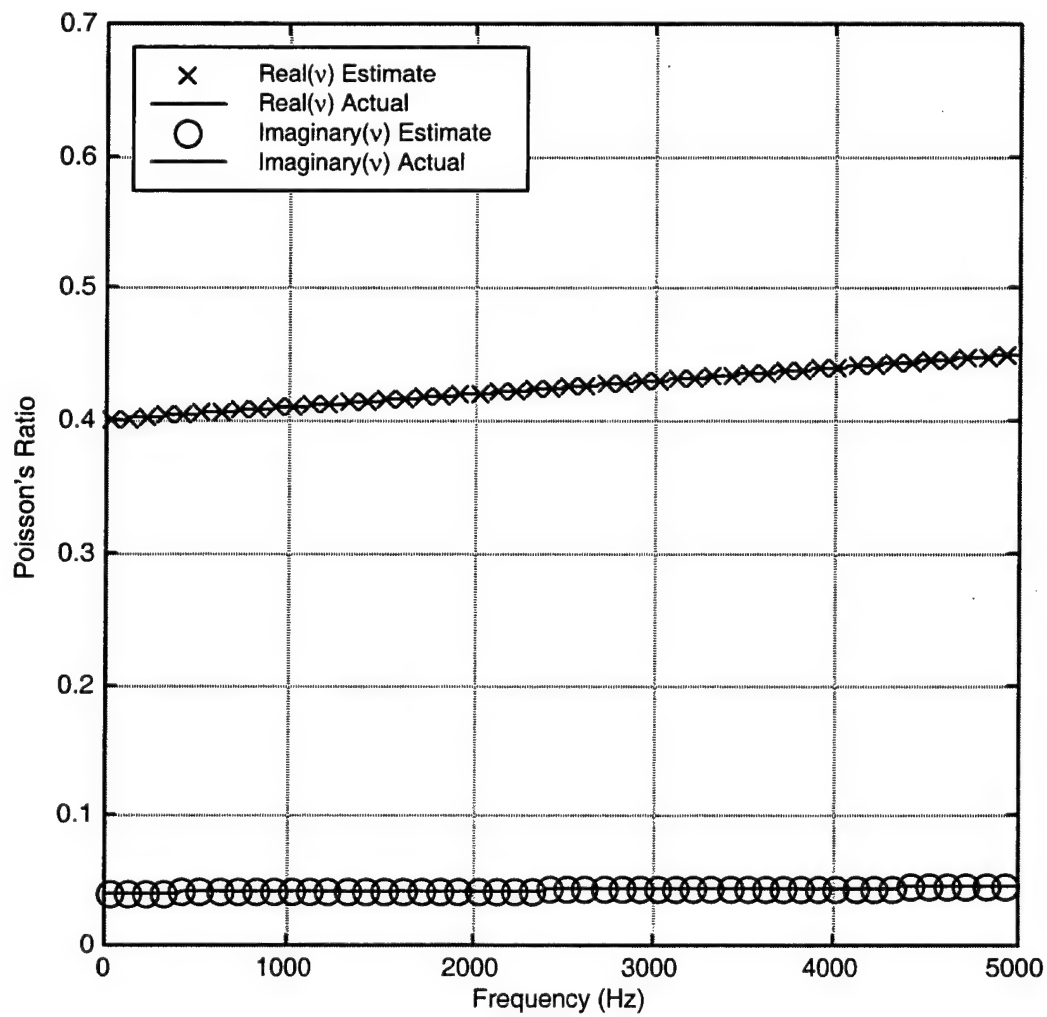


**Figure 17. Real and Imaginary Poisson's Ratio Values  
Calculated Without Noise Versus Frequency**

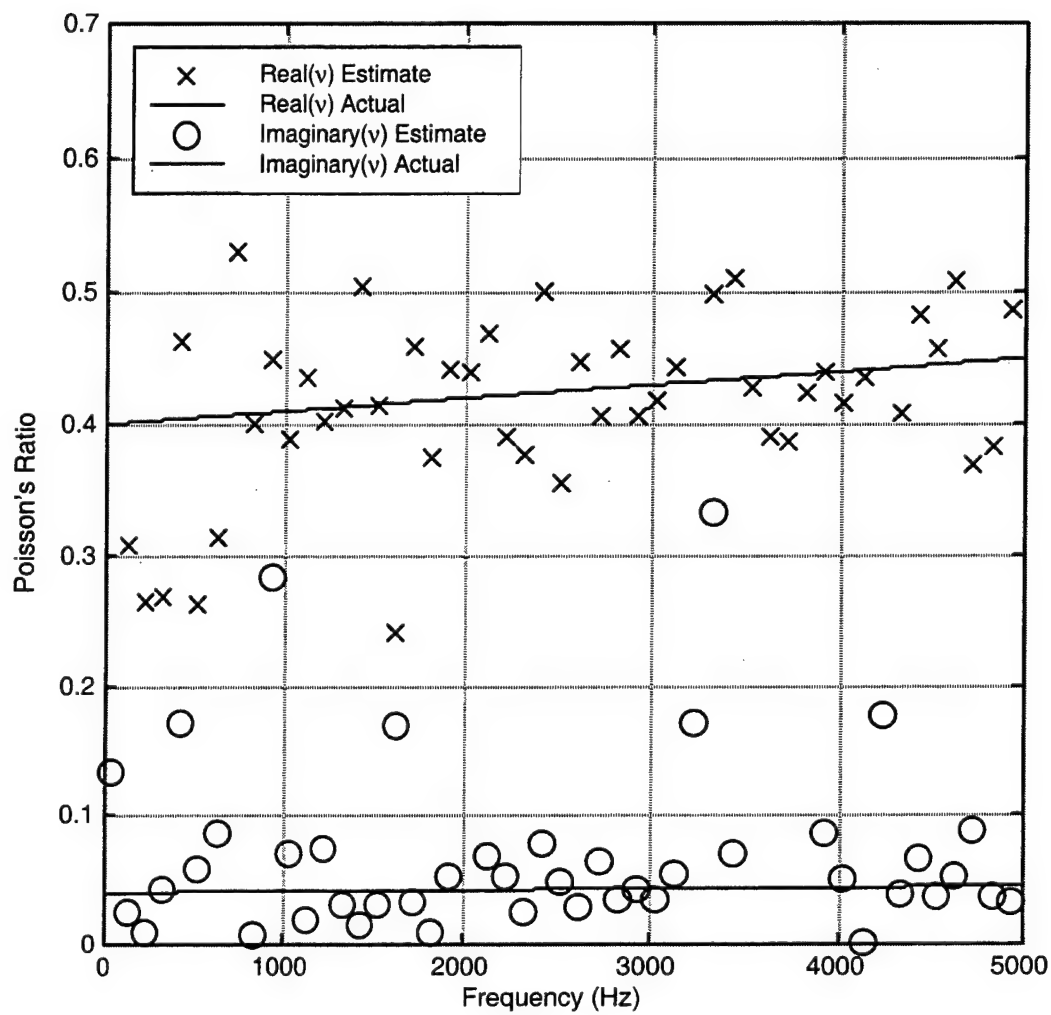


**Figure 18. Real and Imaginary Poisson's Ratio Values  
Calculated With Noise Versus Frequency**

**Table 5. Transfer Function Error Versus Poisson's Ratio Estimation Error**

<b>Transfer Function Error (<math>e</math>)</b>	<b>Estimation Error (<math>\epsilon</math>)</b>
0	0
0.005	0.024
0.010	0.047
0.015	0.069
0.020	0.092
0.025	0.108
0.030	0.125
0.035	0.144
0.040	0.155
0.045	0.169
0.050	0.182

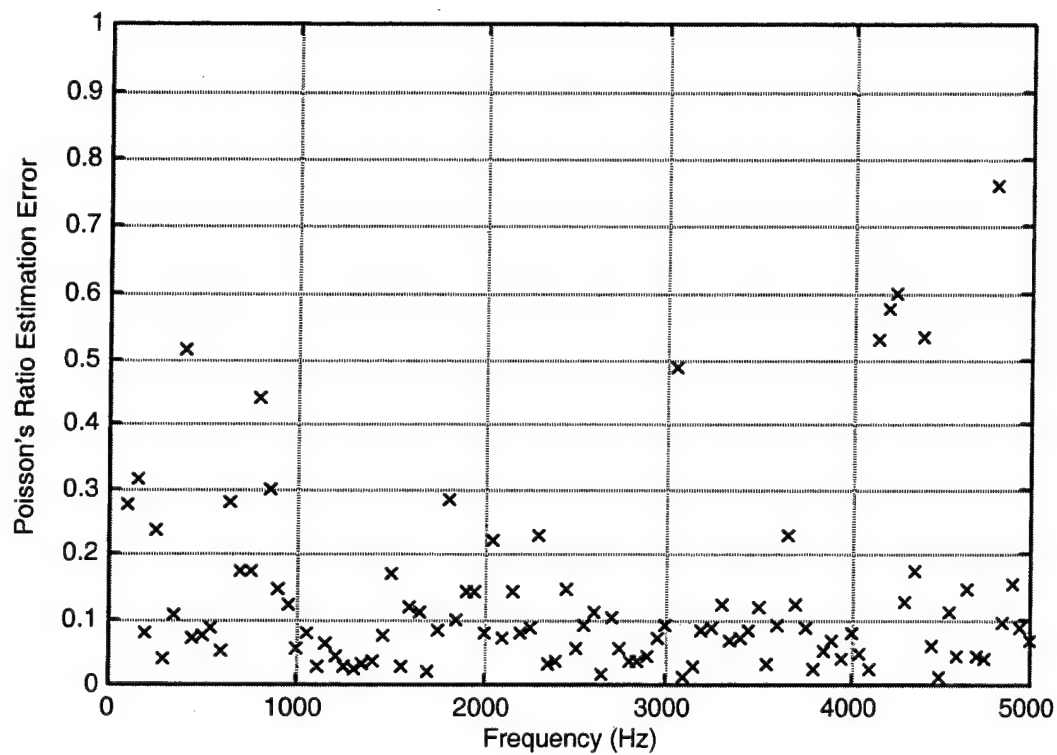


**Figure 19. Poisson's Ratio Estimation Error ( $\epsilon$ ) Versus Frequency**

## 7. CONCLUSIONS AND RECOMMENDATIONS

This report has presented an innovative method for measuring the complex Young's modulus, complex shear modulus, and complex Poisson's ratio of a viscoelastic cylinder. The new nonresonant technique is based on measured transfer functions that are obtained by vibrating the cylinder linearly and rotationally with two different-size masses on its free end. Both masses have their own individual transfer functions, which can be measured on a spectrum analyzer and combined to yield the unknown Young's modulus and shear modulus values at every frequency where a measurement is made. Once these moduli are determined, Poisson's ratio can be calculated.

This new method is particularly beneficial because it measures Young's modulus and the shear modulus at every frequency where a transfer function measurement is made without relying on system resonances or curve fitting to transfer functions. Rather, the calculation from transfer function measurement to the calculation of moduli is exact (i.e., no error is introduced). Moreover, Monte Carlo numerical simulations show that this method is relatively unaffected by noise introduced during the transfer function measurement.

It is suggested that future work include laboratory experiments to verify that the closed-form, nonresonant method can be applied to actual physical problems.



## 8. REFERENCES

1. D. M. Norris, Jr., and W. C. Young, "Complex Modulus Measurements by Longitudinal Vibration Testing," *Experimental Mechanics*, vol. 10, 1970, pp. 93-96.
2. W. M. Madigosky and G. F. Lee, "Improved Resonance Technique for Materials Characterization," *Journal of the Acoustical Society of America*, vol. 73, no. 4, 1983, pp. 1374-1377.
3. S. L. Garrett, "Resonant Acoustic Determination of Elastic Moduli," *Journal of the Acoustical Society of America*, vol. 88, no. 1, 1990, pp. 210-220.
4. I. Jimeno-Fernandez, H. Überall, W. M. Madigosky, and R. B. Fiorito, "Resonance Decomposition for the Vibratory Response of a Viscoelastic Rod," *Journal of the Acoustical Society of America*, vol. 91, no. 4, part 1, April 1992, pp. 2030-2033.
5. G. F. Lee and B. Hartmann, "Material Characterizing System," U.S. Patent 5363701, 15 November 1994.
6. G. W. Rhodes, A. Migliori, and R. D. Dixon, "Method for Resonant Measurement," U.S. Patent 5495763, 5 March 1996.
7. R. F. Gibson and E. O. Ayorinde, "Method and Apparatus for Non-Destructive Measurement of Elastic Properties of Structural Materials," U.S. Patent 5533399, 9 July 1996.
8. B. J. Dobson, "A Straight-Line Technique for Extracting Modal Properties from Frequency Response Data," *Mechanical Systems and Signal Processing*, vol. 1, 1987, pp. 29-40.
9. C. Minas and D. J. Inman, "Matching Finite Element Models to Modal Data," *Journal of Vibration and Acoustics*, vol. 112, no. 1, 1990, pp. 84-92.

10. T. Pritz, "Transfer Function Method for Investigating the Complex Modulus of Acoustic Materials: Rod-Like Specimen," *Journal of Sound and Vibration*, vol. 81, 1982, pp. 359-376.
11. W. M. Madigosky and G. F. Lee, "Instrument for Measuring Dynamic Viscoelastic Properties," U.S. Patent 4352292, 5 October 1982.
12. W. M. Madigosky and G. F. Lee, "Method for Measuring Material Characteristics," U.S. Patent 4418573, 6 December 1983.
13. B. Lundberg and R. H. Blanc, "Determination of Mechanical Properties from the Two-Point Response of an Impacted Linearly Viscoelastic Rod Specimen," *Journal of Sound and Vibration*, vol. 126, 1988, pp. 97-108.
14. B. Lundberg and S. Ödeen, "In Situ Determination of the Complex Modulus from Strain Measurements on an Impacted Structure," *Journal of Sound and Vibration*, vol. 167, 1993, pp. 413-419.
15. W. Madigosky, "In Situ Dynamic Material Property Measurement System," U.S. Patent 5365457, 15 November 1994.

## INITIAL DISTRIBUTION LIST

Addressee	No. of Copies
Office of Naval Intelligence (ONI 241 – J. Zilius, R. Melusky)	2
Office of Naval Research (ONR 321 – D. Davidson, R. Elswick)	2
Defense Technical Information Center	2
Michigan State University (C. Radcliffe)	5